Actin-modulated nuclear shape controls adaptive reprogramming in cancer-associated fibroblasts

Keywords: Cancer-associated fibroblast, Tumor microenvironment, Melanoma, BRAF inhibitor, β-catenin.

Authors: Jie Wang[1], Bruna da Silva Soley[1], Yao Xiao[1], Lindsey G. Siegfried[1], Linli Zhou[1], Mingang Xu[2,3], Sarah E. Millar[2, 3, 4, 5], Thomas Andl[6, $,] Yuhang Zhang[1*]

Affiliations:

1. Division of Pharmaceutical Sciences, College of Pharmacy, University of Cincinnati, Cincinnati, OH, USA

2. Black Family Stem Cell Institute, Icahn School of Medicine at Mount Sinai, New York, NY 10029, USA

3. Department of Cell, Developmental and Regenerative Biology, Icahn School of Medicine at Mount Sinai, New York, NY 10029, USA

4. Department of Oncological Sciences, Icahn School of Medicine at Mount Sinai, New York, NY 10029, USA

5. Tisch Cancer Institute, Icahn School of Medicine at Mount Sinai, New York, NY 10029, USA.

6. Stravitz-Sanyal Institute for Liver Disease and Metabolic Health Virginia Commonwealth University, Richmond, VA, USA

[$] **Previous address:** Burnett School of Biological Sciences, University of Central Florida, Orlando, FL 32816

*Corresponding author: Yuhang Zhang, E-mail address: zhang2y4@ucmail.uc.edu

*Corresponding author address: University of Cincinnati, College of Pharmacy, Division of Pharmaceutical Sciences, Cincinnati, Ohio, United States. Phone number: + 1 513-558-0740

SUMMARY

Cancer-associated fibroblasts (CAFs) adapt to external cues such as therapeutic agents and extracellular matrix (ECM) stiffness in the tumor microenvironment (TME) through a reprogramming process. Here, we show that BRAF inhibitors (BRAFis) drive accumulation of nuclear β-catenin in CAFs by inducing actin-mediated deformation of the nucleus. Exposure to stiff substrates can also lead CAFs to undergo cytoskeletal reorganization and exert forces on the nucleus, allowing β-catenin to enter the nucleus and reprogram its transcriptional activities. Mechanistically, BRAFi accelerates RAS-dependent RAF kinase transactivation by binding to the BRAF and CRAF kinase domains, accelerating BRAF and CRAF homo and heterodimerization and phosphorylation. Subsequently, RAF activation initiates downstream ERK signaling, which simultaneously inactivates GSK-3β and stimulates Rho kinase (ROCK) signaling. Notably, ablating RAS and RAF isoforms as well as pharmacological blockade of ROCK activity effectively suppressed BRAFi-induced nuclear deformation and β-catenin entry in CAFs, further confirming that the ROCK-cytoskeleton axis mediates BRAFi-driven RAF activation and nuclear import of β-catenin for reprogramming. Thus, ROCK-regulated actin polymerization is a master CAF response pathway that can be stimulated by external signals to reprogram the transcriptional activity of CAFs by enhancing nuclear β-catenin transport through a noncanonical mechanical mechanism.

INTRODUCTION

Cancer-associated fibroblasts (CAFs) are a major stromal component within the tumor microenvironment (TME) and play crucial roles in cancer progression, metastasis, and therapy resistance[1]. Originating from resident fibroblasts, mesenchymal stem cells, or other progenitor cells, CAFs exhibit a distinct phenotype characterized by the expression of biomarkers such as α-smooth muscle actin (α-SMA), fibroblast activation protein (FAP), and platelet-derived growth factor receptor β (PDGFR-β)[2-4]. CAFs possess diverse functions, including extracellular matrix (ECM) deposition and remodeling, growth factor secretion, and extensive signaling exchange with tumor cells and with other stromal cells[4].

One of the most significant breakthroughs in treating metastatic melanoma has been the identification of mutations in the B-Raf proto-oncogene, serine/threonine kinase (BRAF) gene[5]. BRAF is normally kept inactive by autoinhibition, a mechanism in which the BRAF regulatory domain blocks the activation of the kinase domain in the absence of upstream RAS signals[6]. The BRAF V600E mutation, a valine-to-glutamic acid substitution at position 600, relieves autoinhibition and releases BRAF from its inactive state without the need for upstream RAS signals, leading to constitutive activation of the mitogen-activated protein kinase/extracellular signal-regulated kinase (MAPK/ERK) signaling pathway[7,8]. The development of mutant BRAF inhibitors (BRAFis), such as vemurafenib and dabrafenib, has provided a targeted therapeutic strategy aimed at inhibiting the aberrant signaling caused by BRAF mutations[9]. BRAFis work by binding to the ATP-binding site in the kinase domain, preventing the enzyme from transferring phosphate groups to downstream signaling molecules and ultimately disrupting the MAPK/ERK signaling pathway[10]. However, despite initial positive outcomes, the emergence of resistance to

BRAFis poses a significant challenge, often leading to disease relapse and progression[11].

CAFs are exposed to a diverse range of cues within the TME, which influence their activation, phenotype, and function, including therapeutic agents, ECM stiffness, and metabolic byproducts. While BRAFis are designed to target BRAF-mutant cancer cells, their off-target effects on stromal cells, including CAFs, which carry wild-type BRAF, are increasingly recognized as critical factors influencing therapeutic success and resistance[12,13]. Recent studies have shown that BRAFis can induce paradoxical effects on the activation of the MAPK/ERK pathway in wild-type BRAF or RAS-mutant cells[14-17]. Several studies suggest that this is due mainly to unintentional RAF dimerization promoted by BRAFis and transactivation[10,18,19]. Notably, BRAFis have been linked to the activation of alternative pathways in CAFs, such as nuclear β-catenin signaling, which consequently enhances the biological properties of CAFs and complicates the therapeutic landscape by fostering a microenvironment that supports tumor progression despite inhibition of BRAF in cancer cells[20]. However, the underlying mechanism remains to be determined.

The interaction between CAFs and BRAFis has revealed a complex relationship that goes beyond merely being bystanders. In this study, we sought to identify the molecular mechanisms by which CAFs respond to external cues and activate nuclear β-catenin signaling. We discovered a mechanical connection between actin remodeling, nuclear deformation, and nuclear β-catenin accumulation for CAF reprogramming. These data suggest that BRAF inhibition promotes the formation of BRAF and CRAF homodimers and heterodimers and activates the ROCK signaling pathway, driving actin cytoskeleton remodeling. We further show that actin cytoskeleton remodeling can also be stimulated by increased matrix stiffness. Furthermore, we explored how

increased nuclear β-catenin influences fibroblast behavior and its effects on melanoma progression.

Our results demonstrate that actin-based nuclear shape regulation is a master regulatory mechanism in CAFs that directs the adaptive reprogramming of CAFs in response to external stimuli. Our data suggest that blockade of this regulatory axis in CAFs could potentially paralyze their functions and increase the efficacy of targeted therapy in melanoma.

MATERIALS AND METHODS

Transgenic mouse strains

Col1α2-CreER mice were kindly provided by Dr. de Crombrugghe[21]. The *tetO-ΔN-β-catenin* transgenic mouse strain was generated in Dr. Sarah Millar's laboratory and was reported in our previous studies[22,23]. The *Rosa-rtTA* (Jax 005670) mouse strains were obtained from the Jackson Laboratory (Bar Harbor, ME, USA). Both mouse strains were backcrossed to the C57BL/6 (B6) genetic background. To generate the triple *Col1α2-CreER*; *Rosa-rtTA*; *tetO-ΔN-β-catenin* mouse strain, *Col1α2-CreER*, *Rosa-rtTA*, and *tetO-ΔN-β-catenin* mice were crossed for several generations. Mice were genotyped by polymerase chain reaction (PCR) analysis of genomic DNA extracted from tail biopsies. The presence of the Cre transgene, *Col1α2-CreER*, was identified by PCR using forward primer: 5′ CGGTCTGGCAGTAAAAACTAT 3′ and reverse primer: 5′ CAGGGTGTTATAAGCAATCCC 3′. The *Rosa-rtTA* allele was genotyped using forward primer: 5′ AAGACCGCGAAGAGTTTGTC 3′ and reverse primer: 5′ AAAGTCGCTCTGAGTTGTTAT 3′. The *ΔN-β-catenin* transgene was genotyped using forward primer: CCTTGTATCACCATGGACCCTCAT and reverse primer: TAGTGGGATGAGCAGCGTCAAACT. Standard PCR cycle protocols were used. Male and female animals were used in the study, and no differences between sexes were observed. All the mice were housed in the Laboratory Animal Services Facility of the University of Cincinnati under an artificial 14 hour/10 hours light-dark cycle and were allowed free access to food and water. The Institutional Animal Care and Use Committee of the University of Cincinnati (IACUC) approved all experimental procedures involving mice (22-08-19-01).

Cell lines

Human melanoma cell lines, including A375 (Cat# CRL-1619) and SK-MEL-24 (Cat# HTB-71), were purchased from American Type Culture Collection (ATCC, Manassas, VA). Two human CAF cell lines, 224350P1 and DT01027P1, which were isolated from surgically excised human melanoma tissues, were obtained from Asterand Bioscience (Detroit, MI) and designated M50 and M27, respectively. Human dermal fibroblasts were provided by Dr. Dorothy Supp in the Department of Surgery at the University of Cincinnati. Murine *Braf*^{V600E}; *Pten*$^{lox5/lox5}$ D4M melanoma cells were purchased from Kerafast (Boston, MA)[24]. Melanoma cell lines were authenticated by ATCC and routinely validated in the laboratory on the basis of the expression of melanoma proteoglycan antigens and surface molecules, including GP100[25], MITF, Melan-A, and tyrosinase[26]. We authenticated CAFs and normal human dermal fibroblasts by evaluating their unique morphological characteristics and the expression of specific skin fibroblast markers, including TE7[27], vimentin, and α-SMA[28]. All cell lines were passaged fewer than 20 times and maintained in Dulbecco's modified Eagle medium (DMEM) supplemented with 10% (v/v) fetal bovine serum (FBS) and 1% (v/v) 10,000 units/mL penicillin, 10,000 μg/mL streptomycin, and 25 μg/mL Amphotericin B in a humidified incubator at 37°C with 5% CO_2. Cells were monitored for mycoplasma contamination routinely via a Universal Mycoplasma Detection Kit. Cell culture reagents were purchased from Corning Life Sciences (Durham, NC) unless otherwise stated. Experimental procedures involving biosafety hazards were carried out under the University of Cincinnati Institutional Biosafety Committee protocol 16-08-17-01.

Mouse primary fibroblast isolation

The sex of neonatal *Col1α2-CreER*, *Rosa-rtTA*, and *TetO-ΔN-β-catenin* mice and littermates was

first determined by genotyping the SRY gene using PCR with forward primer: 5' TTGTCTAGAGAGCATGGAGGGCCATGTCAA 3' and reverse primer: 5' CCACTCCTCTGTGACACTTTAGCCCTCCGA. To isolate dermal fibroblasts, the dorsal skin of sex-matched 2–3-day-old littermates was collected, and subcutaneous fat and other tissues were removed from the dermal side. The skin was floated with the epidermis facing up in 0.25% trypsin solution at 37°C for one hour to separate the dermis and epidermis. The dermis was minced into small pieces of approximately 1 mm^2 using sterile scissors. The dermal pieces were then incubated in 5 mL of 2.5 mg/mL collagenase IV solution for a total of 30 minutes at 37°C with pipetting every 10 minutes. After 30 minutes, 5 mL of DMEM was added to stop the digestion. The dermal cell suspension was filtered through 70 μm and 40 μm strainers to remove cell clumps and undissociated tissues. Fibroblasts were collected by centrifugation at 1500 rpm for five minutes and resuspended in 10 mL of DMEM for culture in a 10 cm dish. Fibroblast genotypes were determined by PCR as described for transgenic mouse strains and validated by immunostaining for the expression of α-SMA, vimentin, S100A4, keratin 14 (negative, keratinocyte marker), and TRP1 (negative, melanocyte marker). A total of four pairs of ΔN-β-catenin-overexpressing mouse fibroblasts and wild-type fibroblasts were isolated and frozen in liquid nitrogen at passages 3-5 for *in vitro* and *in vivo* studies.

Induction of ΔN-β-catenin expression in cultured mouse fibroblasts

To activate CreER- and rtTA-dependent ΔN-β-catenin expression in isolated mouse fibroblasts, 3×10^5 cells were seeded in a 10 cm dish and treated with 4-hydroxytamoxifen (4-OHT; Sigma–Aldrich, Cat# H6278) at a final concentration of 0.2 μg/mL and doxycycline (Dox; Sigma–Aldrich, Cat# 33429) at 1.25 μg/mL for 72 hours. Following induction, the cells were washed with PBS

and harvested for subsequent assays.

Cell proliferation assay

1×10^5 Dox-treated mouse fibroblasts of the genotypes *Col1α2-CreER; Rosa-rtTA*; *TetO-ΔN-β-catenin* or *Col1α2-CreER; Rosa-rtTA* were seeded and cultured in a 6-cm dish. On days three, five, and seven, the cells were collected, and the number of cells was counted via a hemocytometer. At least three repeats were included for each indicated cell line three times. Cell number counting was performed at least three times for statistical analysis.

Collagen gel contraction assay

Dox-treated 5×10^4 mouse fibroblasts of the genotypes *Col1α2-CreER; Rosa-rtTA*; *TetO-ΔN-β-catenin* or *Col1α2-CreER*; *Rosa-rtTA* were suspended in 500 µL of 1 mg/mL rat tail collagen type I in DMEM and seeded in one well of a 24-well tissue culture plate. After a 30-minute incubation in a humidified incubator at 37°C, 1 mL of fresh medium was added to the top of the gel for incubation. After a 72-hour incubation, the gel was detached from the wall of each well and allowed to contract as indicated. Pictures of the gels were taken using a Nikon digital camera every 24 hours, and ImageJ software (NIH, Bethesda, MD) was used to measure the area of the gel. Gel contraction was calculated as the percentage reduction in the gel area from 0 to 72 hours: gel contraction (%) = [(area at 0 h - area at 72 h)/area at 0 h] × 100.

Confocal reflection microscopy (CRM)

5×10^4 Dox-treated mouse fibroblasts of the genotypes *Col1α2-CreER; Rosa-rtTA*; *TetO-ΔN-β-catenin* or *Col1α2-CreER*; *Rosa-rtTA* were embedded in collagen gels in the same way as

described for the collagen gel contraction assay. After a 72-hour incubation, the gels were collected, and the collagen fiber distribution and organization were directly examined using a Zeiss LSM 710 confocal microscope at 40X magnification. Images were acquired at a depth of at least 100 μm below the top surface of the gel to minimize edge effects. Pictures of at least ten areas of each gel were randomly captured for 3D reconstruction using ImageJ. Fiber connectivity and spacing mean were calculated using ImageJ with the BoneJ plugin (http://bonej.org).

Mouse melanoma induction

As shown in Fig. 4A, two groups of melanomas were generated by injecting intradermally a mixture of 1 x 10^5 D4M melanoma cells and 1 x 10^5 uninduced mouse fibroblasts of genotype *Col1α2-CreER; Rosa-rtTA*; *TetO-ΔN-β-catenin* or *Col1α2-CreER; Rosa-rtTA* into the flanks of 5-week-old B6 mice. For each group, a minimum of three male and three female mice were used as recipient mice. The mice were monitored daily after cell injection for tumor formation. After the tumors reached a volume of approximately 62.5 mm^3 (marked as day one), to induce β-catenin overexpression in *Col1α2-CreER; Rosa-rtTA*; *TetO-ΔN-β-catenin* fibroblasts, all mice were fed a Dox diet (Bio-Serv, F-4096) and underwent intraperitoneal injection of 10 mg/mL tamoxifen (Sigma–Aldrich, St. Louis, MO) in corn oil at 1 mg/g body weight for seven consecutive days. Afterwards, the size of the tumors was measured using a caliper every other day for 18 days. The tumor volume was calculated using the following formula: $[(\text{width})^2 \times (\text{length})]/2$. The mice were euthanized around day 18 when the tumor size exceeded 15% of the body size, and the tumors were harvested for analysis. The number of mice used in each study was calculated using power analysis. Specific randomization and blinding were not necessary for the reported study. Student's t-test was used to determine the significance of the differences in tumor size and weight between

the two groups.

Histology, immunofluorescence staining, and immunohistochemistry

The collected melanoma tissues were fixed in 10% formalin overnight at 4°C and embedded in paraffin for sectioning. Five μm-thick paraffin-embedded tumor tissue sections were prepared for hematoxylin and eosin (H&E) staining and immunostaining as described previously[20,29]. For histological analysis, paraffin sections were stained using a standard H&E staining protocol, mounted with VectaMount permanent mounting medium (Vector Labs, Burlingame, CA), and analyzed using a Nikon Eclipse 80i fluorescence microscope.

For immunostaining, paraffin sections were deparaffinized, rehydrated, and then unmasked in citrate buffer (pH 6.0) using the microwave heating method. After washing with PBS, the sections were blocked in 10% bovine serum albumin (BSA) and subsequently incubated with each primary antibody at 4°C overnight. The following primary antibodies were used: anti-α-SMA (Thermo Fisher, clone 1A4, 1:200), anti-fibronectin (Millipore, clone F3648, 1:200), anti-Ki67 (Thermo Fisher, clone 27309-1-AP, 1:50), and anti-cyclin D1 (Thermo Fisher, clone SP4, 1:50). After incubation with primary antibodies, the slides were washed with PBS three times, incubated with the corresponding biotin-conjugated secondary antibodies at room temperature for one hour, washed again three times with PBS, and then incubated with either fluorochrome-conjugated streptavidin for immunofluorescence or VECTASTAIN Elite ABC Reagents (Vector Laboratories, Burlingame, CA) for immunohistochemistry. Nuclei were counterstained with DAPI (blue) for immunofluorescence or hematoxylin (blue) for immunohistochemistry. Images were taken using a Nikon Eclipse 80i fluorescence microscope.

The numbers of positively stained cells (α-SMA+, Ki67+, Cyclin D1+) or α-SMA- melanoma cells in each high-power field (40X) were counted using the particle analysis function of ImageJ. The number of cells per square millimeter was calculated by multiplying the number of cells counted in each field by 4.5. The fibronectin+ area in each high-power field (40X) was measured using ImageJ. Fibronectin+ (%) was calculated by dividing the fibronectin+ area by the area of the entire field. For each melanoma sample, at least 12 randomly selected fields were counted. A minimum of three independent experiments were performed for each immunostaining quantification.

Collagen staining

Picrosirius red staining was performed using Picro-Sirius red stain kit according to the manufacturer's instructions (American MasterTech, Lodi, CA). Briefly, paraffin sections of mouse melanomas were dewaxed, hydrated, and stained in picrosirius red for one hour. After staining, the tissue sections were washed with 1% acetic acid for one minute, dehydrated in 100% ethanol, cleared in xylene, and mounted with VectaMount permanent mounting medium (Vector Laboratories) for evaluation.

Quantification of collagen content

Paraffin sections were deparaffinized and rehydrated for collagen content quantification using the Sirius Red/Fast Green Collagen Staining Kit (Chondrex, Cat# 9046) following the manufacturer's instructions. Briefly, after the slide was incubated with the dye solution at room temperature for 30 minutes, the dye solution was removed, and the slide was rinsed with distilled water until the

water became colorless. One milliliter of dye extraction buffer was added to each slide to elute the dye from the dyed tissues. The optical absorbances at 540 nm and 605 nm were measured using a microplate reader. The collagen content was calculated using the following formula: Collagen (μg/section) = [OD540 − (OD605 × 0.291)]/0.0378. Three tissue sections per group were used for quantification and statistical analysis.

Generation of transgene-expressing human CAF lines

To immortalize M27 and M50, Lenti-SV40 lentivirus (ABM, Cat# G203) was purchased from Applied Biological Materials (Richmond, Canada). The immortalized cell lines were named iM27 and iM50. All BRAF and CRAF constructs, including Flag-tagged BRAF (BRAF_OHu28570C_pGenlenti_N-FLAG), Myc-tagged BRAF (HygR_BRAF_OHu28570C_pGenlenti_N-MYC), BRAF-T529N (BRAF-T529N_OHu28570C_pGenlenti_N-FLAG), Flag-tagged CRAF (HygR_RAF1_OHu28584C_pGenlenti_N-Flag), Myc-tagged CRAF (RAF1_OHu28584C_pGenlenti_N-MYC), and CRAF-T421N (RAF1-T421N_OHu28584C_pGenlenti_N-MYC), were designed and cloned by GenScript (Piscataway, NJ). All the constructs were generated by inserting their respective transgene fragments into the pGenlenti backbone. Respective lentiviruses were produced at the Cincinnati Children's Hospital Viral Vector Core using the BRAF and CRAF constructs described above.

For lentiviral transduction, 5×10^4 immortalized CAFs were seeded in one well of a 6-well plate. When the cells reached 50% confluence, 50 μl of virus was mixed with 450 μl of basal DMEM supplemented with 10 μg/mL polybrene (Santa Cruz, sc-134220) and added. After a 16-hour

incubation, the virus medium was replaced with 2 mL of fresh DMEM supplemented with 10% FBS for cell culture. Depending on the antibiotic resistance gene cloned in each lentiviral construct, transduced cells were selected with 10 μg/mL puromycin (Gibco, A11138--03), 50 μg/mL hygromycin B, or 10 μg/mL blasticidin (Santa Cruz Biotechnology, sc-495389). The cells were incubated with antibiotics for 7 days and then changed to normal DMEM.

siRNA transfection

Silencer® siRNAs targeting ARAF (ID: 153), BRAF (ID:507), CRAF (ID: 1548), NRAS (ID: 120250), KRAS (ID: 120703), HRAS (ID 120898), and scramble Silencer® siRNA control (Cat# 4390843) were purchased from Thermo Fisher Scientific (Rochester, NY). For CAFs expressing BRAF-WT or BRAF(T529N), cells were transfected with FlexiTube siRNAs targeting BRAF (ID: 673) to silence endogenous BRAF expression. For CAFs expressing CRAF-WT or CRAF(T421N), cells were transfected with FlexiTube siRNAs targeting CRAF (ID: 5894) to silence endogenous CRAF expression. FlexiTube siRNAs targeting the 3′ untranslated region (3′ UTR) of BRAF and CRAF were obtained from Qiagen (Hilden, Germany)

Briefly, 1×10^5 CAFs were seeded in one well of a 6-well tissue culture plate and allowed to grow until approximately 80% confluence. Prior to transfection, the culture medium was replaced with fresh DMEM. The cells were then transfected with the indicated siRNAs using Lipofectamine RNAiMAX (Thermo Fisher, Rochester, NY). For each transfection, a siRNA-Lipofectamine mixture was prepared by incubating 9 μL of Lipofectamine RNAiMAX and 30 pmol of the indicated siRNA in 300 μL of DMEM at room temperature for 5 minutes. The cells in each well were then incubated with the siRNA-Lipofectamine mixture for 48 hours at 37°C in a humidified

incubator with 5% CO_2. Afterward, the transfection mixture was replaced with DMEM. To silence NRAS, KRAS, and HRAS expression in CAFs, three siRNAs targeting NRAS, KRAS, and HRAS (30 pmol each as described above) were mixed and incubated with 9 μL of Lipofectamine RNAiMAX in 300 μL of DMEM for transfection.

CAF treatment

To treat CAFs with small-molecule compounds, 5×10^3 iM27 or iM50 cells were seeded in each well of an 8-well Nunc™ Lab-Tek™ II chamber slide (Thermo Fisher Scientific, Rochester, NY) and cultured for three days. The cells were treated as indicated: 2 μM PLX4032 for 72 hours; 0.5 μM GSK2118436 for 72 hours; 50 nM jasplakinolide for 2 hours; 500 nM cytochalasin D for 24 hours; 10 μM Y-27632 for 24 hours; and 10 μM HA-1077 for 24 hours or 0.5 μM SCH772984 for 24 hours. Following treatment, the cells were subjected to immunofluorescence staining directly on the slides.

Chamber slide immunofluorescence staining

After treatment, the cells in each chamber were fixed in 4% paraformaldehyde for 10 minutes at room temperature and then permeabilized with 0.05% Triton X-100 for 10 minutes on ice for immunofluorescence staining. After permeabilization, the cells were washed three times with PBS and blocked in 10% BSA for one hour at room temperature. Primary antibodies for SUN2 (Millipore, HPA001209, 1:200), Nesprin-2 (Abcam, clone EPR28137-54, 1:200), lamin A/C (Proteintech, 10298-1-AP, 1:200), F-actin (Thermo Fisher, clone R415, 1:200), β-catenin (Thermo Fisher, clone 15B8, 1:500), paxillin (BD Biosciences, clone 349, 1:200), and α-SMA (Thermo Fisher, clone 1A4, 1:200) were then added to each chamber and incubated overnight at 4°C. The

next day, after washing with PBS three times, an Alexa Fluor 488- or 594-conjugated secondary antibody (Thermo Fisher, Rochester, NY) was added to the corresponding well for a one-hour incubation at room temperature. Slides were counterstained with Hoechst 33342 (Hoechst), mounted with VECTASHIELD Antifade Mounting Medium (Vector Laboratories, Burlingame, CA), and coverslipped. Images were acquired using a Nikon Eclipse 80i fluorescence microscope or a Zeiss LSM 710 confocal microscope. To measure the nuclear β-catenin intensity, the nuclei were stained with Hoechst at a concentration of 10 μg/mL for 10 minutes at room temperature. Nuclei were identified on the basis of Hoechst fluorescence, and the β-catenin signal within these regions was quantified using ImageJ.

Cell stiffness experiments

To evaluate how CAFs respond to stiff matrix environments, CAFs were cultured for 24 hours on soft slides with either 0.2 kPa or 50 kPa stiffness (Matrigen, Irvine, CA). Cell culture and treatment, as well as immunofluorescence staining, were performed using the same protocols as those described above.

Proximity ligation assay (PLA)

PLA was performed using the Duolink® *In Situ* Red Starter Kit (DUO92101, Millipore, Burlington, MA) according to the manufacturer's instructions. Briefly, 0.5×10^4 cells were cultured in each well of an 8-well Nunc™ Lab-Tek™ II chamber slide. After being cultured for three days under the indicated conditions, the cells were fixed in 4% paraformaldehyde for 10 minutes at room temperature and permeabilized with 0.1% Triton X-100 in PBS for 10 minutes on ice. Afterwards, the cells were blocked with Duolink blocking solution for one hour at 37°C

and then incubated overnight at 4°C with the following primary antibodies: BRAF (Proteintech, 20899-1-AP), CRAF (Proteintech, clone 1D6A1), FLAG (Proteintech, 20543-1-AP), or MYC (Proteintech, clone 1A5A2). The next day, the slides were washed with wash buffer A and incubated with species-specific PLA probes (PLUS and MINUS) for one hour at 37°C. After probe incubation, the cells were washed twice with wash buffer A for 5 minutes each. Ligation-ligase solutions were then added to each well and incubated at 37°C for 30 minutes to ligate the two probes into a circular DNA template. The cells were subsequently washed twice with wash buffer A for two minutes each. The circular templates were amplified by adding polymerase in amplification buffer containing nucleotides and fluorescently labeled oligonucleotides, resulting in distinct fluorescent spots. The slides were then mounted with Duolink *in* situ mounting medium containing DAPI for 30 minutes and imaged using a Nikon Eclipse 80i fluorescence microscope. PLA signals were quantified using ImageJ as either the average dot intensity per 40X field or the number of dots per cell.

Coimmunoprecipitation (co-IP)

Co-IP was performed using a Pierce Crosslink Immunoprecipitation Kit according to the manufacturer's instructions (Thermo Fisher, Waltham, MA). Briefly, 10 μg of Myc-tag antibody (Proteintech, clone 1A5A2) or mouse IgG (Thermo Fisher, 31903) was added to a spin column containing 20 μL of resin slurry in a 1.5 mL collection tube. The antibody and beads were incubated at room temperature with gentle rotation for one hour. After incubation, the spin columns were centrifuged, and the antibody-bound resin was subsequently rinsed with 1X coupling buffer three times to remove unbound antibodies. A 2.5 mM disuccinimidyl suberate (DSS) crosslinker solution was added to crosslink the antibody to the resin. Subsequently, 1 mg of

protein extracted from the cells co-expressing Flag-tagged CRAF and Myc-tagged CRAF with or without PLX4032 treatment was added to a spin column and incubated with rotation at 4°C overnight. After incubation, the column was washed three times with 1X TBS and one time with 1X conditioning buffer. Samples were eluted in 50 μL of elution buffer. The eluate was boiled with sample buffer at 95°C for five minutes for Western blotting.

Western blotting

For Western blotting, 20 × 10^4 iM27 or iM50 cells were seeded in one 10 cm culture dish and treated as described above for three days. After treatment, proteins were extracted using RIPA buffer supplemented with Halt Protease and Phosphatase Inhibitor Cocktail, EDTA-free (Thermo Fisher, 78443). Briefly, the cells were lysed in RIPA buffer on ice for 30 minutes with brief vortexing every 10 minutes. The lysates were then centrifuged at 15,000 × g for 15 minutes at 4°C, and the supernatants were collected and transferred to fresh tubes. Protein was quantified using the BCA protein assay (Thermo Fisher, A55860). 20 μg of protein was loaded per lane and run on a 10-12% SDS–PAGE gel and subsequently transferred to a nitrocellulose membrane. The membranes were blocked with 5% fat-free milk or 5% BSA in TBST for one hour at room temperature and then incubated with the following primary antibodies: ARAF (Cell Signaling Technology, 4432, 1:1000), BRAF (Proteintech, 20899-1-AP, 1:1000), CRAF (Proteintech, clone 1D6A1, 1:1000), CRAF (Proteintech, 26863-1-AP, 1:1000), phospho-BRAF (Cell Signaling Technology, 2696, 1:1000), phospho-CRAF (Cell Signaling Technology, 9127, 1:1000), Flag (Proteintech, 20543-1-AP, 1:1000), MYC (Proteintech, clone 1A5A2, 1:1000), MYC (Cell Signaling Technology, clone 71D10, 1:1000), KRAS (Proteintech, 12063-1-AP, 1:1000), HRAS (Proteintech, 18295-1-AP, 1:1000), NRAS (Proteintech, 10724-1-AP, 1:1000), ERK1/2 (Cell

Signaling Technology, clone 3A7, 1:1000), and phospho-ERK (Cell Signaling Technology, clone D13.14) in blocking buffer. After being washed three times with TBST, the membranes were then incubated with IRDye 800CW donkey anti-rabbit IgG secondary antibody (LI-COR, 926–32213, 1:2000) or IRDye 680RD donkey anti-mouse IgG secondary antibody (LI-COR, 926–68072, 1:2000) at a 1:2000 dilution in blocking buffer and washed three times with TBST. The membranes were imaged using the Odyssey CLx imaging system (LI-COR, model #9140).

Quantification of nuclear morphology

First, 0.5×10^4 CAFs were seeded in one well of an 8-well chamber slide and treated as indicated in each figure. Following treatment, the nuclei were stained with Hoechst, and confocal images of randomly selected fields were captured at 40X magnification using the Zeiss LSM 710 confocal microscope. Hoechst-stained images were analyzed using ImageJ software. Aspect ratio and circularity of individual nuclei were quantified using the Analyze Particles function.

Actin cap quantification

A total of 0.5×10^4 CAFs seeded in one well of an 8-well chamber slide were stained for F-actin using Phalloidin Labeling Probes (Thermo Fisher, R415, 1:200), and nuclei were stained with Hoechst. Confocal images of randomly selected fields were acquired at 40X magnification using a Zeiss LSM 710 confocal microscope. The actin caps were identified as dense F-actin fibers spanning over the apical surface of the nucleus. The intensity of F-actin staining of the actin caps was quantified using ImageJ.

Z-stack confocal microscopy

To visualize the three-dimensional organization of the actin caps relative to the nucleus, Z-stack images were acquired at 40X magnification using the Zeiss LSM 710 confocal microscope. Hoechst staining was used to define the nuclear boundaries. A single cell was scanned from the bottom to the top of the nucleus at 1 μm intervals, covering the entire nuclear volume.

Quantification and statistical analysis

Data were analyzed using the GraphPad Prism 9 software package (GraphPad Software Inc., San Diego, CA) and expressed as the mean ± SD. The mean difference was determined by Student's t-tests and considered statistically significant at $P < 0.05$.

RESULTS

BRAFi induces nuclear deformation in CAFs

β-catenin is a dual-function protein that functions in cell adhesion at the cellular membrane and also mediates signaling by shuttling between the cytoplasm and the nucleus. Previously, we reported that BRAFi induces noncanonical activation of nuclear β-catenin signaling in CAFs[20]. Nuclear morphological changes are a known mechanism by which cells regulate gene expression[30]. To understand how BRAFi influences β-catenin cellular localization, we first examined the nuclear shape of CAFs upon treatment with PLX4032 (Fig. 1) and GSK2118436 (Fig. S1). As shown in Figs. 1A and S1A, the nuclei in many BRAFi-treated CAFs became elongated. The average nuclear aspect ratio in BRAFi-treated CAFs, which was calculated by dividing the length of the longest axis of the nucleus by the length of its shortest axis, was ~1.94, compared with ~1.39 in DMSO-treated CAFs (Figs. 1B and S1B), suggesting that BRAFi stretched the nuclei in CAFs. Furthermore, nuclear circularity, which represents the roundness of a nucleus, was reduced in BRAFi-treated CAFs to ~0.63 from ~0.77 in DMSO-treated CAFs (Figs. 1C and S1C). These findings indicate that BRAFi caused the nuclei in CAFs to lose their typical shapes.

Nuclear shape and positioning are regulated by the linker of the nucleoskeleton and cytoskeleton (LINC) complex, which connects the nucleus (nucleoskeleton) to the cytoskeleton[31]. Alterations in the LINC complex in BRAFi-treated CAFs were visualized by immunofluorescence staining of two core LINC components, Nesprin-2 and SUN2. Nesprin-2 is anchored in the outer nuclear membrane and interacts with actin filaments, thereby joining the cytoskeleton to the nucleoskeleton. As shown in Figs. 1D and S1D, Nesprin-2 in CAFs extend into the cytoplasm. This structural arrangement enables the LINC complex to sense and transmit mechanical and

signaling cues from the cytoplasm to the nucleus. Interestingly, upon BRAFi treatment, the cytoplasmic localization of Nesprin-2 surrounding the nucleus was increased in CAFs. SUN2 is a membrane-embedded protein located in the inner nuclear membrane, where it interacts with nuclear lamins such as lamin A/C. BRAFi-treated CAFs presented aberrant nuclear distribution of SUN2, suggesting disruption of the LINC complex and possible compromise of the nuclear envelope (Figs. 1E and S1E). Since the nuclear membrane was disrupted, we next investigated whether there were changes in nuclear lamins, as they are directly connected to the inner nuclear membrane and are essential structural proteins[32]. Discontinuous staining of lamin A/C in BRAFi-treated CAFs confirmed structural breakdown of the nuclear lamin structure (Figs. 1F and S1F). These findings suggest that changes in the LINC complex may contribute to nuclear deformation in CAFs because the complex transmits mechanical forces between the cytoskeleton and the nucleus.

Mechanical association between actin polymerization and nuclear deformation leads to noncanonical β-catenin nuclear accumulation

Actin polymerization, particularly around the nucleus, plays an important role in regulating the LINC complex and nuclear shape[33]. Increased actin polymerization exerts mechanical force on the nucleus and can cause nuclear rupture. To understand whether the BRAFi-induced changes in the LINC complex and nuclear elongation observed in CAFs were caused by actin-mediated nuclear force, we next investigated changes in actin filament organization in PLX4032-treated CAFs. As shown in Fig. 2A-B and S2A-D, polymerized actin filaments were greater in CAFs than in normal dermal fibroblasts. However, the actin structures were much more prominent in CAFs treated with PLX4032 (Fig. 2C-D and S2E-F), suggesting that BRAFi induced cytoskeleton remodeling in

CAFs. We focused on the perinuclear actin cap, a specialized subset of actin filaments that span the nucleus[34], because it is directly anchored to the LINC complexes on the nuclear envelope. Z-stack confocal imaging revealed prominent assembly of actin cap structures in PLX4032-treated CAFs, where F-actin aligned above the nucleus in a dome-like structure and colocalized with nuclear staining, as indicated by the yellow arrow (Fig. S2G).

The above observations suggest that mechanical forces exerted by enhanced actin cytoskeleton remodeling induced by BRAFi may contribute to nuclear deformation and increased nuclear β-catenin entry in CAFs. To test this hypothesis, we treated CAFs with jasplakinolide (Jaspla), an actin polymerization inducer known to promote cytoskeletal remodeling[35]. As hypothesized, Jaspla treatment led to nuclear deformation (Fig. 2E). Consistent with PLX4032 treatment, Jaspla-treated CAFs presented an increase in the nuclear aspect ratio from ~1.30 to 1.69 and a reduction in circularity from ~0.83 to 0.68, indicating that the nuclei became elongated and less round (Fig. 2F). Moreover, actin polymerization and the formation of perinuclear actin caps were significantly increased in Jaspla-treated CAFs (Fig. 2G-H). These findings confirm that increased cytoskeletal remodeling is directly responsible for nuclear deformation and β-catenin accumulation in both BRAFi-treated and Jaspla-treated CAFs.

Next, we investigated whether inhibiting actin polymerization can reverse the changes in nuclear shape and β-catenin nuclear entry induced by PLX4032. To this end, CAFs were treated with PLX4032 alone or in combination with cytochalasin D (CytoD), an actin polymerization inhibitor[36]. Notably, PLX4032-induced nuclear deformation was significantly reversed by CytoD, with the nuclear aspect ratio decreasing to approximately 1.50 and the nuclear circularity

increasing to approximately 0.81 (Fig. 2I-J). F-actin staining confirmed the reductions in actin fiber polymerization and actin cap structure formation in CAFs treated with PLX4032 + CytoD together compared to those treated with PLX4032 only (Fig. 2K-L), indicating effective disruption of actin filament assembly caused by PLX4032 following CytoD treatment.

Similarly, confocal imaging of SUN2-stained CAFs revealed that the nuclear distribution of SUN2 in Jaspla-treated CAFs was similar to that observed in PLX4032-treated CAFs, with increased nuclear β-catenin accumulation (Fig. 2M-N). In contrast, abnormal SUN2 localization in PLX4032-treated CAFs was diminished by simultaneous CytoD treatment (Fig. 2O). Consequently, CytoD also suppressed nuclear β-catenin accumulation in PLX4032-treated CAFs (Fig. 2P). These data demonstrate that PLX4032-induced nuclear deformation and β-catenin nuclear transport are driven by increased cytoskeletal remodeling.

Matrix stiffness deforms the nucleus and regulates β-catenin nuclear entry

ECM stiffness can significantly remodel the actin cytoskeleton by exerting forces on cells through integrin receptors[37]. Because increased tissue stiffness is a classic characteristic of solid tumors, we next tested whether elevated matrix stiffness could promote nuclear deformation and β-catenin nuclear translocation by inducing actin polymerization. CAFs were cultured on either soft substrate with a stiffness of 0.2 kPa or hard substrate with a stiffness of 50 kPa. Consistent with PLX4032 stimulation, increased ECM stiffness led to an increased aspect ratio and decreased nuclear circularity, suggesting nuclear elongation and deformation. However, CytoD reversed the nuclear morphological changes induced by high stiffness, with the aspect ratio reduced to approximately 1.53 and the circularity restored to approximately 0.76 (Fig. 3A-C). Confocal imaging of F-actin

revealed a marked increase in actin polymerization and actin cap formation in CAFs cultured on hard substrate compared with those cultured on soft substrate (Fig. 3D-E). However, this effect was abolished by CytoD, which had the same effect on PLX4032 stimulation (Fig. 2K). In parallel, the abnormal nuclear localization of SUN2 observed on hard substrates was also rescued by CytoD (Fig. 3F). Importantly, the increased nuclear accumulation of β-catenin in CAFs cultured on hard substrate compared with soft substrate was significantly reduced by CytoD (Fig. 3G–H). These findings suggest that ECM stiffness triggers nuclear deformation and subsequent β-catenin accumulation by driving cytoskeleton remodeling, representing a common mechanism of mechanotransduction by which CAFs respond to a stiffer tumor microenvironment.

Nuclear β-catenin accumulation induces fibroblast reprogramming

Nuclear β-catenin is crucial for regulating the expression of genes that are essential for cell proliferation, differentiation, and survival. Since β-catenin is shuttled into the nucleus by various stimuli, including BRAFi and stiff substrates, we wanted to understand the biological outcome of increased nuclear β-catenin in fibroblasts and in melanoma development. As shown in Fig. S3A, B, fibroblasts overexpressing a constitutively active form of β-catenin (*Col1α2-CreER^{T2}; Rosa-rtTA; TetO-ΔN-β-catenin*, hereafter ΔN-β-catenin) displayed stronger nuclear β-catenin expression than control fibroblasts expressing endogenous β-catenin (*Col1α2-CreER^{T2}; Rosa-rtTA*, hereafter control). These ΔN-β-catenin-overexpressing fibroblasts exhibited increased proliferation (Fig. S3C) and elevated expression of α-SMA, which is a well-established CAF marker (Fig. S3D-E). Furthermore, the expression and distribution of paxillin and F-actin were upregulated in ΔN-β-catenin-expressing fibroblasts (Fig. S3F-I). Since changes in the actin cytoskeleton and scaffolding proteins such as paxillin are often linked to cell contractility, we

assessed their contractile capacity using the gel contraction assay and confocal reflection microscopy (CRM) (Fig. S3J-N). The results showed that ΔN-β-catenin-expressing CAFs exhibited increased contractility. These data demonstrate that the increase in nuclear β-catenin activity enhances the biological properties of fibroblasts.

Next, to investigate the importance of ΔN-β-catenin-expressing CAFs in *in vivo* melanoma development, we co-injected fibroblasts and BRAF-mutant D4M melanoma cells intradermally into B6 mice to induce melanoma formation (Fig. 4A). Melanomas containing ΔN-β-catenin-expressing CAFs (ΔN-β-catenin melanomas) grew faster than melanomas containing wild-type CAFs at each time point (Fig. 4B). On day 18, when tumors were collected, melanomas containing ΔN-β-catenin-expressing CAFs were larger and weighed more than control melanomas (Fig. 4C-D), suggesting that upregulated β-catenin activity in CAFs promoted melanoma growth *in vivo*. H&E staining revealed that the structure of the ΔN-β-catenin melanomas was more compact with fewer intercellular spaces than that of the control tumors (Fig. 4E). To confirm this observation, we assessed the expression of two major proliferation markers, Ki67 and Cyclin D1. As shown in Fig. 4F, G, the number of Ki67+ melanoma cells (α-SMA-) was notably increased in ΔN-β-catenin melanomas, suggesting that upregulated β-catenin activity in CAFs promoted the proliferative activity of BRAF-mutant melanoma cells. In line with this observation, increased expression of Cyclin D1 was detected in ΔN-β-catenin melanomas (Fig. 4H, I).

Increased α-SMA expression was observed in these melanomas, indicating that upregulated β-catenin activity drove CAF activation (Fig. 4J, K), which is consistent with the *in vitro* data showing that β-catenin overexpression promoted fibroblast proliferation (Fig. S3C). CAFs are the

major producers of ECM components, such as fibronectin and collagen, which play critical roles in remodeling the TME and promoting tumor malignancy. Increased fibronectin and collagen deposition were found in ΔN-β-catenin melanomas (Fig. 4L-O). In conclusion, increased nuclear β-catenin, which can be driven by BRAFi or a stiff TME, reprograms CAFs and promotes their activation, playing a critical role in promoting matrix remodeling and melanoma progression.

BRAFi binds to the RAF kinase domain and promotes BRAF and CRAF dimerization and phosphorylation

Next, we sought to understand how BRAFi drives cytoskeleton reorganization and leads to nuclear deformation and β-catenin nuclear entry in CAFs. The RAF kinase family includes three serine/threonine-specific protein kinases, ARAF, BRAF, and CRAF[38]. We used small interfering RNA (siRNA) to selectively silence each RAF kinase to identify which RAF isoform mediates the response to PLX4032 in CAFs (Fig. 5A). As shown in Fig. 5B, C, ARAF depletion had no significant effect on the PLX4032-induced nuclear accumulation of β-catenin compared with that in mock-infected controls. In contrast, the loss of either BRAF or CRAF markedly suppressed β-catenin nuclear entry in response to PLX4032. These findings were confirmed in additional CAF lines (Fig. S4A–C). Together, the observations indicate that BRAF and CRAF, but not ARAF, are involved in mediating the nuclear accumulation of β-catenin driven by BRAFi in CAFs.

The activation of RAF isoforms is intrinsically linked to their ability to form dimers, either as homodimers (e.g., BRAF-BRAF or CRAF-CRAF) or heterodimers (e.g., BRAF-CRAF), depending on the cellular context. To understand how BRAFi induces paradoxical RAF activation in CAFs, we first examined RAF dimerization via proximity ligation assay (PLA). PLA revealed

greater BRAF-CRAF heterodimer formation in PLX4032-treated CAFs than in control cells (Figs. 5D, E and S4D, E). To investigate RAF homodimer formation in CAFs, we co-expressed Flag-tagged BRAF and Myc-tagged BRAF to identify BRAF-BRAF homodimerization and, in a separate set of cells, co-expressed Flag-tagged CRAF and Myc-tagged CRAF to assess CRAF-CRAF homodimerization. PLX4032 treatment notably enhanced the formation of both BRAF-BRAF and CRAF-CRAF homodimers (Fig. 5F-I). In addition, the formation of BRAF and CRAF dimers was confirmed using another BRAFi, GSK2118436 (Fig. S4F-I). Coimmunoprecipitation (co-IP) with an anti-Myc antibody further confirmed increased CRAF homodimerization, as well as increased heterodimerization, in PLX4032-treated CAFs co-expressing Flag- and Myc-tagged CRAF (Fig. 5J). Additionally, phosphorylation of BRAF at Ser445 and CRAF at Ser338—both established markers of RAF activation—was elevated in CAFs following PLX4032 treatment (Fig. 5K). Together, these findings suggest that BRAFi promotes RAF activation in CAFs by increasing both RAF dimerization and phosphorylation.

In melanoma cells harboring the BRAF V600E mutation, PLX4032 binds to the kinase domain of mutant BRAF to block its enzymatic activity because the mutation effectively releases the autoinhibition. However, whether PLX4032 binding to the kinase domains of wild-type BRAF and CRAF is required for increased RAF dimerization remains unclear. To address this, we generated two mutant CAF lines expressing gatekeeper mutations in the kinase domain of BRAF and CRAF that prevent BRAFi access to their ATP-binding pockets[39]: one line expressing BRAF(T529N) and another expressing CRAF(T421N). In both lines, endogenous BRAF or CRAF was selectively depleted (Fig. S5A, S5D). Depletion of endogenous BRAF or CRAF significantly reduced nuclear β-catenin accumulation in control CAFs (siBRAF and siCRAF) and in CAFs

expressing the respective gatekeeper mutants BRAF (T529N) and CRAF (T421N) upon PLX4032 treatment but not in CAFs expressing wild-type BRAF (BRAF-WT) or CRAF (CRAF-WT) (Fig. S5B, C, E, F). Notably, PLX4032 and GSK2118436 failed to induce BRAF-CRAF heterodimer formation in CAFs expressing either BRAF (T529N) or CRAF (T421N) (Fig. S6). As expected, PLX4032 did not promote phosphorylation at BRAF Ser445 or CRAF Ser338 in these gatekeeper mutant lines because of the inhibition of BRAF and CRAF dimerization (Fig. 5L, M). Together, these findings demonstrate that the direct binding of BRAFi to the kinase domains of BRAF or CRAF is a key step for RAF dimerization, activation, and downstream nuclear accumulation of β-catenin in CAFs.

BRAFi-induced RAF dimerization is RAS dependent

RAFs are mediators between RAS-GTPases and downstream MEK and ERK kinases. In wild-type RAF cells, RAS binding to the RAS-binding domain (RBD) and the cysteine-rich domain (CRD) of RAF is essential for RAF activation because the binding effectively eliminates autoinhibition and facilitates RAF dimerization and transactivation. To determine whether RAS binding is still required for BRAFi binding and BRAFi-induced RAF dimerization and transactivation, we depleted all RAS isoforms in CAFs using siRNA (Fig. 6A). PLA revealed that the PLX4032-induced increase in BRAF-CRAF heterodimer formation was markedly reduced in RAS-depleted CAFs compared with mock-transfected cells (Figs. 6B and S7A). In line with this, the phosphorylation of BRAF at Ser445 and CRAF at Ser338 was not elevated following PLX4032 treatment in RAS-depleted cells (Fig. 6C), confirming that RAS is involved in BRAFi-driven RAF dimerization and phosphorylation.

We next examined whether disruption of the RAS-RAF signaling axis affects cytoskeletal

remodeling, nuclear morphology, and β-catenin nuclear accumulation. RAS-depleted CAFs reversed PLX4032-induced nuclear deformation, with the nuclear aspect ratio returning to ~1.44 and the circularity increasing to ~0.81 (Fig. 6D-F). Similarly, confocal imaging of F-actin expression and distribution revealed that PLX4032-induced actin polymerization and actin cap formation were suppressed upon RAS depletion (Fig. 6G-I). In addition, the abnormal cytosolic redistribution of Nesprin-2 observed after PLX4032 treatment was reversed in RAS-depleted cells (Fig. 6J). As a result, the increased nuclear accumulation of β-catenin induced by PLX4032 was significantly diminished in RAS-depleted CAFs, as measured by the average intensity of nuclear β-catenin (Fig. 6K-L). We further validated these findings in iM50 CAFs, which produced similar results (Fig. S8). These findings confirmed that RAS binding to wild-type BRAF and CRAF and removing autoinhibition in the kinase domains are essential for the acceleration of RAF dimerization and transactivation in CAFs by BRAFis.

ROCK signaling is downstream of RAF activation and regulates cytoskeletal reorganization and β-catenin nuclear translocation

The ROCK signaling pathway plays a crucial role in regulating the actin cytoskeleton. To assess possible molecular interaction between the RAS-RAF signaling pathway and ROCK signaling, we first evaluated the activation of ERK, which is an established downstream effector of RAF kinases[40], in response to increasing PLX4032 and GSK2118436 concentrations in two CAF lines. The results showed that BRAFi treatment led to increased ERK phosphorylation (Figs. 7A and S9A-C). This response was diminished upon RAS depletion (Figs. 7B and S9D), confirming that RAS is the upstream activator of the BRAFi-induced RAF-ERK pathway. Furthermore, PLX4032 did not promote ERK phosphorylation in cells expressing BRAFi-resistant BRAF (T529N) or

CRAF (T421N) mutants, indicating that BRAFi-driven RAF activation is necessary for the activation of downstream ERK signaling (Fig. 7C-D). Interestingly, GSK-3β phosphorylation at Serine 9 was significantly increased in CAFs upon PLX4032 treatment (Fig. S9E), which indicates that GSK-3β inactivation may contribute to nuclear β-catenin accumulation.

Notably, we also observed activation of the ROCK pathway following PLX4032 treatment. MYPT1, a well-known substrate of ROCK that regulates actin contraction and relaxation, was phosphorylated upon PLX4032 exposure (Fig. 7E), which inhibited its activity and sustained the phosphorylation of MLC, promoting actin filament polymerization and contraction. This response was diminished by cotreatment with the ERK inhibitor SCH772984 (SCH) (Fig. 7F), demonstrating that ROCK acts downstream of the RAF-ERK pathway to promote actin polymerization. Immunostaining of β-catenin further revealed that the PLX4032-induced increase in nuclear β-catenin was reduced by ERK inhibition (Fig. S9F-G). These results suggest that β-catenin translocation to the nucleus is a ROCK-dependent process.

Next, we investigated whether inhibiting ROCK signaling could reverse the effects of PLX4032 on nuclear deformation and β-catenin nuclear accumulation. To this end, CAFs were cotreated with PLX4032 and a well-established ROCK inhibitor Y27632. PLX4032-induced nuclear deformation was reversed by Y27632 treatment, as demonstrated by the restoration of nuclear morphology, with the nuclear aspect ratio returning to ~1.50 and the circularity increasing to ~0.78 (Fig. 7G-I). Compared with those of PLX4032 alone, F-actin staining confirmed effective actin cytoskeletal disruption and diminished actin cap formation under the combined treatment (Fig. 7J-K). This observation confirms that PLX4032-induced actin cap formation depends on the

activation of the ROCK pathway. Furthermore, the aberrant nuclear distribution of SUN2 triggered by PLX4032 was rescued in CAFs treated with Y27632 (Fig. 7L). As expected, the increased nuclear accumulation of β-catenin induced by PLX4032 was significantly reduced with ROCK inhibition (Fig. 7M, N). The effects of Y27632 in reversing PLX4032-induced nuclear deformation, actin polymerization, and nuclear β-catenin accumulation were confirmed by using another ROCK inhibitor, HA-1077, and in extra CAF lines (Fig. S10).

We further tested whether CAFs respond to ECM stiffness and undergo nuclear deformation through a similar mechanism. CAFs seeded on hard substrate with a stiffness of 50 kPa were treated with Y27632 and HA-1077. Upon treatment, nuclear deformation was reversed, with the nuclear aspect ratio reduced to ~1.55 and the circularity increased to ~0.78 (Figs. 8A-C and S11A-C). Confocal imaging revealed a remarkable loss of cytoskeletal actin fibers and actin cap structures upon ROCK inhibition (Figs. 8D-E and S11D-G). The aberrant nuclear distribution of SUN2 induced by stiffness was reversed in Y27632-treated CAFs (Fig. 8F). Importantly, the increased nuclear translocation of β-catenin observed in CAFs cultured on stiff substrates was markedly reduced following Y27632 or HA-1077 treatment (Figs. 8G-H and S11H-K). Collectively, these findings indicate that the ROCK pathway acts as a key signal mediator, allowing CAFs to respond to BRAFi and stiffness, and inducing transcriptional regulation by modulating cytoskeletal remodeling, nuclear deformation, and β-catenin nuclear accumulation.

DISCUSSION

Our results reveal a major mechanism by which CAFs respond to and adapt to BRAFi by reprogramming their transcriptional activities. Mechanistically, BRAFi induces RAF-ROCK activation, cytoskeletal remodeling, and nuclear deformation in CAFs, leading to increased nuclear β-catenin accumulation due to disruption of the nuclear membrane structure. β-catenin is a key mediator of Wnt/β-catenin signaling pathway, which plays a crucial role in the transcriptional regulation needed for many biological processes, including cell fate decisions, tissue development, and cancer progression. In our study, both *in vitro* and *in vivo* data revealed that β-catenin functions as a key driver of CAFs in melanoma and promotes their biological properties, suggesting a novel mechanism by which CAFs undergo nuclear β-catenin-driven reprogramming in response to BRAFi through changes in the nuclear shape and membrane.

The nucleus, which is encircled by a double-layered membrane, quickly responds to both intrinsic and extrinsic cues in a tightly controlled manner by regulating protein transport through nuclear pore complexes. However, β-catenin does not possess a traditional nuclear localization signal. There are two potential mechanisms for β-catenin nuclear entry. First, β-catenin may directly interact with the nuclear pore complex and pass through the membrane. Second, β-catenin may enter the nucleus through binding to other nuclear proteins, such as TCF/LEF transcription factors. Though we cannot fully exclude the possibility that β-catenin could be shuttled into the nucleus by other nuclear proteins in BRAFi-treated CAFs, our data suggest that BRAFi-induced nuclear deformation and resulting disruption of the nuclear pore structure are a major reason for increased β-catenin nuclear transport. Another factor that may add to increased β-catenin nuclear presence is increased GSK-3β phosphorylation and inactivation, which contributes to β-catenin stabilization

for increased nuclear entry.

Increased stiffness is a common characteristic of metastatic tumors. We found that exposure to a stiff matrix induces nuclear deformation and nuclear β-catenin accumulation in CAFs. Nuclear morphology can vary widely and is influenced by factors such as mechanical forces, cytoskeletal tension, molecular signals, and cellular cues to preserve nuclear functionality. Nuclear pores are large, multiprotein structures within the nuclear membrane that transport molecules between the cytoplasm and nucleus. Thus, changes in nuclear shape and nuclear membrane tension can alter the diameter of nuclear pores. We observed that in both BRAFi-treated CAFs and stiff matrix-stimulated CAFs, the nuclei were elongated, which can lead to membrane rupture and expansion of the nuclear pores, facilitating the nuclear import of regulatory molecules, e.g., β-catenin. β-catenin signaling triggered by nuclear stretch is important because it allows different signals to stimulate the same cellular outcome in CAFs, which may enable the cells to react to diverse environmental events more efficiently.

Intriguingly, the mechanism by which BRAFi and a stiff environment lead to nuclear deformation is unknown. The transmembrane LINC complexes mechanically connect lamins and chromatin inside the nucleus to the cytoskeleton outside the nucleus[41]. This connection is essential for maintaining nuclear shape and structure and transmitting mechanical forces inside the nucleus. Furthermore, actin polymerization drives the formation of actin caps that specifically influence nuclear shape and positioning. We consistently observed increased actin polymerization and actin cap presence, disorganized SUN2 and Nesprin-2 localization, and elongated nuclei in BRAFi-treated CAFs, suggesting that BRAFi-driven actin polymerization exerts mechanical forces to

deform the nucleus through disruption of the LINC complex.

The rearrangement and assembly of the actin cytoskeleton not only control cell shape, polarity, and migration but also influence cell metabolism. Increased actin polymerization was observed in CAFs exposed to either BRAFi or a stiff matrix, although the stimulatory mechanisms may differ (Fig. 8). Actin polymerization is regulated by the ROCK signaling pathway. While matrix stiffness can activate ROCK signaling through integrin receptors on the cell membrane[42], our findings reveal a novel signaling mechanism through which BRAFi induces the abnormal activation of RAF kinases in CAFs, leading to the activation of the ROCK signaling pathway. We confirmed that ERK signaling functions downstream of the RAS/RAF axis in CAFs upon BRAFi treatment. The activation of ERK signaling has multiple effects, as it can activate the ROCK pathway and inactivate GSK-3β by phosphorylation. These data further confirm that CAFs respond to various extracellular cues and reprogram their biological properties through ROCK-driven cytoskeletal reorganization.

Although BRAFi was designed to inhibit mutant BRAF carrying the V600E point mutation by inserting in the mutant kinase domain and blocking the active site, it has been shown that it can paradoxically activate the MAPK/ERK pathway in cells carrying wild-type BRAF. However, how CAFs react to BRAFis and change their behavior in melanoma remain unknown. Our data revealed that both BRAF and CRAF function in BRAF-wild-type CAFs. Further investigation demonstrated that BRAFi accelerates BRAF and CRAF dimerization and phosphorylation in CAFs through a RAS-dependent and kinase domain-mediated mechanism. Another potential promoting mechanism is that BRAFi in BRAF-wild-type CAFs can stabilize BRAF and CRAF dimers.

Theoretically, the increased RAF activity explains the observation that the ERK and ROCK pathways are activated in CAFs by BRAFi, contributing to increased actin polymerization, which acts on the nucleus.

The opposite effects by BRAFis, promoting wild-type BRAF kinase activity while inhibiting the mutant BRAF kinase, can be attributed to the BRAF mutation and the steric conformation of the kinase domains (Fig. 9). In wild-type monomeric BRAF, binding of the N-terminal RBD and CRD to the C-terminal kinase domain blocks the access of kinase to either kinase substrates or small-molecule compounds, such as BRAFis, which can only be released by RAS binding. However, in the BRAF V600E mutant, this specific substitution within the activation loop in the kinase domain disrupts autoinhibition, leading to its constitutive activation even as a monomer without RAS binding. The differences in their acting mechanisms suggest the steric conformations of wild-type kinase domain and mutant kinase domain are different, which may determine the distinct responses to BRAFis by wild-type and mutant BRAFs. Notably, BRAFi was designed to fit in the mutant BRAF kinase domain and block its catalytic activity. However, in RAF-wild-type CAFs, although BRAFi can gain access to the kinase domains in BRAF and CRAF after RAS binds to the RBD and CRD domains and release autoinhibition, it induces unexpected conformational changes in the kinase domains and promotes their dimerization and transactivation instead.

Given the role of CAFs in promoting melanoma progression and therapy resistance, these cells represent potential therapeutic targets; however, strategies for specifically targeting CAFs are lacking. Our study reveals a new regulatory mechanism in CAFs that allows the cells to react to external cues, including therapeutic agents and stiff stroma, by converging on a common response

pathway involving alterations in nuclear shape and mechanosensation (Fig. 8). The identified ROCK-cytoskeleton axis persistently stimulates CAFs and activates their transcriptional programs by allowing transcription factors to enter the nucleus. The outcomes are multifold, as shown in *in vitro* and *in vivo* β-catenin overexpression experiments. Importantly, these data suggest that disrupting the ROCK pathway and inhibiting actin polymerization could have important therapeutic benefits. ROCK signaling inhibition can suppress the ability of CAFs to respond to a variety of forces and signals in the melanoma microenvironment, ranging from BRAFi to stiff matrix and matrix proteins, and blocks the shuttling of key transcription factors into the nucleus. Exploiting the integral role of ROCK signaling in RAS-RAF and the mechanosignaling of CAFs could lead to a better definition of drug targets that interact with specific signals that maintain and stimulate tumor growth-promoting CAFs.

ETHICAL APPROVAL

The Institutional Animal Care and Use Committee of the University of Cincinnati (IACUC) approved all experimental procedures involving mice under the protocol 22-08-19-01.

ACKNOWLEDGMENTS

We thank Dr. Dorothy Supp for providing human dermal fibroblasts. This work was supported by NIH R01 CA249737 (YZ), and the Center for Clinical & Translational Science & Training (CCTST) Just-In-Time Core Grant (YZ), the UCCC Pilot Project Award Program (YZ), and the Marlene Harris Ride Cincinnati Cancer Pilot Program (YZ). The CCTST Just-In-Time Core Grant was supported by the National Center for Advancing Translational Sciences of the National Institutes of Health under Award Number UL1TR001425. The content is solely the responsibility of the authors and does not necessarily represent the official views of the NIH.

AUTHOR CONTRIBUTIONS

Y.Z. designed the experiments; J.W., B.S., Y.X. and L.Z. performed the experiments and collected the data; J.W., B.S., Y.X., L.Z. and Y.Z. analyzed the data; S.E.M and M.X. provided mouse models; J.W., Y.Z. and T.A. wrote the main manuscript text; J.W. and Y.Z. prepared the figures; J.W., L.Z., Y.Z., L.S., S.E.M. and T.A. reviewed and edited the manuscript. All the authors reviewed and approved the final version to be published. All authors agree to be accountable for all aspects of the work in ensuring that questions related to the accuracy or integrity of any part of the work are appropriately investigated and resolved and declare confidence in the integrity of the contributions of their coauthors.

CONFLICTS OF INTEREST

The authors declare that they have no competing interests.

REFERENCES

1. Wang, X., Zhou, Y., Wang, Y., Yang, J., Li, Z., Liu, F., Wang, A., Gao, Z., Wu, C., and Yin, H. (2025). Overcoming cancer treatment resistance: Unraveling the role of cancer-associated fibroblasts. Journal of the National Cancer Center. 10.1016/j.jncc.2025.03.002.
2. Han, C., Liu, T., and Yin, R. (2020). Biomarkers for cancer-associated fibroblasts. Biomark Res *8*, 64. 10.1186/s40364-020-00245-w.
3. Nurmik, M., Ullmann, P., Rodriguez, F., Haan, S., and Letellier, E. (2020). In search of definitions: Cancer-associated fibroblasts and their markers. Int J Cancer *146*, 895-905. 10.1002/ijc.32193.
4. Liu, T., Zhou, L., Li, D., Andl, T., and Zhang, Y. (2019). Cancer-Associated Fibroblasts Build and Secure the Tumor Microenvironment. Front Cell Dev Biol *7*, 60. 10.3389/fcell.2019.00060.
5. Davies, H., Bignell, G.R., Cox, C., Stephens, P., Edkins, S., Clegg, S., Teague, J., Woffendin, H., Garnett, M.J., Bottomley, W., et al. (2002). Mutations of the BRAF gene in human cancer. Nature *417*, 949-954. 10.1038/nature00766.
6. Park, E., Rawson, S., Li, K., Kim, B.W., Ficarro, S.B., Pino, G.G., Sharif, H., Marto, J.A., Jeon, H., and Eck, M.J. (2019). Architecture of autoinhibited and active BRAF-MEK1-14-3-3 complexes. Nature *575*, 545-550. 10.1038/s41586-019-1660-y.
7. Trebino, T.E., Markusic, B., Nan, H., Banerjee, S., and Wang, Z. (2023). Unveiling the domain-specific and RAS isoform-specific details of BRAF kinase regulation. Elife *12*, RP88836. 10.7554/eLife.88836.

8. Cantwell-Dorris, E.R., O'Leary, J.J., and Sheils, O.M. (2011). BRAFV600E: implications for carcinogenesis and molecular therapy. Mol Cancer Ther *10*, 385-394. 10.1158/1535-7163.MCT-10-0799.

9. Agianian, B., and Gavathiotis, E. (2018). Current Insights of BRAF Inhibitors in Cancer. J Med Chem *61*, 5775-5793. 10.1021/acs.jmedchem.7b01306.

10. Singh, A.K., Sonawane, P., Kumar, A., Singh, H., Naumovich, V., Pathak, P., Grishina, M., Khalilullah, H., Jaremko, M., Emwas, A.H., et al. (2023). Challenges and Opportunities in the Crusade of BRAF Inhibitors: From 2002 to 2022. ACS Omega *8*, 27819-27844. 10.1021/acsomega.3c00332.

11. Bryant, C.J., Keyse, S.M., and Caunt, C.J. (2014). BRAF inhibitor resistance: are holidays and cocktails the answer? Pigment Cell Melanoma Res *27*, 693-695. 10.1111/pcmr.12291.

12. Gibney, G.T., Messina, J.L., Fedorenko, I.V., Sondak, V.K., and Smalley, K.S. (2013). Paradoxical oncogenesis--the long-term effects of BRAF inhibition in melanoma. Nature reviews. Clinical oncology *10*, 390-399. 10.1038/nrclinonc.2013.83.

13. Weeraratna, A.T. (2012). RAF around the edges--the paradox of BRAF inhibitors. N Engl J Med *366*, 271-273. 10.1056/NEJMe1111636.

14. Halaban, R., Zhang, W., Bacchiocchi, A., Cheng, E., Parisi, F., Ariyan, S., Krauthammer, M., McCusker, J.P., Kluger, Y., and Sznol, M. (2010). PLX4032, a selective BRAF(V600E) kinase inhibitor, activates the ERK pathway and enhances cell migration and proliferation of BRAF melanoma cells. Pigment Cell Melanoma Res *23*, 190-200. 10.1111/j.1755-148X.2010.00685.x.

15. Paraiso, K.H., Fedorenko, I.V., Cantini, L.P., Munko, A.C., Hall, M., Sondak, V.K., Messina, J.L., Flaherty, K.T., and Smalley, K.S. (2010). Recovery of phospho-ERK

activity allows melanoma cells to escape from BRAF inhibitor therapy. Br J Cancer *102*, 1724-1730. 10.1038/sj.bjc.6605714.

16. Wang, T., Xiao, M., Ge, Y., Krepler, C., Belser, E., Lopez-Coral, A., Xu, X., Zhang, G., Azuma, R., Liu, Q., et al. (2015). BRAF Inhibition Stimulates Melanoma-Associated Macrophages to Drive Tumor Growth. Clin Cancer Res *21*, 1652-1664. 10.1158/1078-0432.CCR-14-1554.

17. Oh, Y.T., Deng, J., Yue, P., and Sun, S.Y. (2016). Paradoxical activation of MEK/ERK signaling induced by B-Raf inhibition enhances DR5 expression and DR5 activation-induced apoptosis in Ras-mutant cancer cells. Scientific reports *6*, 26803. 10.1038/srep26803.

18. Poulikakos, P.I., Zhang, C., Bollag, G., Shokat, K.M., and Rosen, N. (2010). RAF inhibitors transactivate RAF dimers and ERK signalling in cells with wild-type BRAF. Nature *464*, 427-430. 10.1038/nature08902.

19. Holderfield, M., Nagel, T.E., and Stuart, D.D. (2014). Mechanism and consequences of RAF kinase activation by small-molecule inhibitors. Br J Cancer *111*, 640-645. 10.1038/bjc.2014.139.

20. Liu, T., Zhou, L., Xiao, Y., Andl, T., and Zhang, Y. (2022). BRAF Inhibitors Reprogram Cancer-Associated Fibroblasts to Drive Matrix Remodeling and Therapeutic Escape in Melanoma. Cancer Res *82*, 419-432. 10.1158/0008-5472.CAN-21-0614.

21. Zheng, B., Zhang, Z., Black, C.M., de Crombrugghe, B., and Denton, C.P. (2002). Ligand-dependent genetic recombination in fibroblasts : a potentially powerful technique for investigating gene function in fibrosis. Am J Pathol *160*, 1609-1617. 10.1016/S0002-9440(10)61108-X.

22. Zhou, L., Xu, M., Yang, Y., Yang, K., Wickett, R.R., Andl, T., Millar, S.E., and Zhang, Y. (2016). Activation of beta-Catenin Signaling in CD133-Positive Dermal Papilla Cells Drives Postnatal Hair Growth. PLoS One *11*, e0160425. 10.1371/journal.pone.0160425.

23. Zhou, L., Yang, K., Carpenter, A., Lang, R.A., Andl, T., and Zhang, Y. (2016). CD133-positive dermal papilla-derived Wnt ligands regulate postnatal hair growth. Biochem J *473*, 3291-3305. 10.1042/BCJ20160466.

24. Jenkins, M.H., Steinberg, S.M., Alexander, M.P., Fisher, J.L., Ernstoff, M.S., Turk, M.J., Mullins, D.W., and Brinckerhoff, C.E. (2014). Multiple murine BRaf(V600E) melanoma cell lines with sensitivity to PLX4032. Pigment Cell Melanoma Res *27*, 495-501. 10.1111/pcmr.12220.

25. Rothberg, B.E., Moeder, C.B., Kluger, H., Halaban, R., Elder, D.E., Murphy, G.F., Lazar, A., Prieto, V., Duncan, L.M., and Rimm, D.L. (2008). Nuclear to non-nuclear Pmel17/gp100 expression (HMB45 staining) as a discriminator between benign and malignant melanocytic lesions. Mod Pathol *21*, 1121-1129. 10.1038/modpathol.2008.100.

26. Sheffield, M.V., Yee, H., Dorvault, C.C., Weilbaecher, K.N., Eltoum, I.A., Siegal, G.P., Fisher, D.E., and Chhieng, D.C. (2002). Comparison of five antibodies as markers in the diagnosis of melanoma in cytologic preparations. American journal of clinical pathology *118*, 930-936. 10.1309/EWK9-LUPR-6BC5-1GXV.

27. Goodpaster, T., Legesse-Miller, A., Hameed, M.R., Aisner, S.C., Randolph-Habecker, J., and Coller, H.A. (2008). An immunohistochemical method for identifying fibroblasts in formalin-fixed, paraffin-embedded tissue. J Histochem Cytochem *56*, 347-358. 10.1369/jhc.7A7287.2007.

28. Maehira, H., Miyake, T., Iida, H., Tokuda, A., Mori, H., Yasukawa, D., Mukaisho, K.I., Shimizu, T., and Tani, M. (2019). Vimentin Expression in Tumor Microenvironment Predicts Survival in Pancreatic Ductal Adenocarcinoma: Heterogeneity in Fibroblast Population. Ann Surg Oncol *26*, 4791-4804. 10.1245/s10434-019-07891-x.

29. Zhou, L., Yang, K., Dunaway, S., Abdel-Malek, Z., Andl, T., Kadekaro, A.L., and Zhang, Y. (2018). Suppression of MAPK signaling in BRAF-activated PTEN-deficient melanoma by blocking beta-catenin signaling in cancer-associated fibroblasts. Pigment Cell Melanoma Res *31*, 297-307. 10.1111/pcmr.12657.

30. Neelam, S., Richardson, B., Barker, R., Udave, C., Gilroy, S., Cameron, M.J., Levine, H.G., and Zhang, Y. (2020). Changes in Nuclear Shape and Gene Expression in Response to Simulated Microgravity Are LINC Complex-Dependent. Int J Mol Sci *21*, 6762. 10.3390/ijms21186762.

31. Cantwell, H., and Dey, G. (2022). Nuclear size and shape control. Semin Cell Dev Biol *130*, 90-97. 10.1016/j.semcdb.2021.10.013.

32. Vahabikashi, A., Adam, S.A., Medalia, O., and Goldman, R.D. (2022). Nuclear lamins: Structure and function in mechanobiology. APL Bioeng *6*, 011503. 10.1063/5.0082656.

33. Davidson, P.M., and Cadot, B. (2021). Actin on and around the Nucleus. Trends Cell Biol *31*, 211-223. 10.1016/j.tcb.2020.11.009.

34. Khatau, S.B., Hale, C.M., Stewart-Hutchinson, P.J., Patel, M.S., Stewart, C.L., Searson, P.C., Hodzic, D., and Wirtz, D. (2009). A perinuclear actin cap regulates nuclear shape. Proceedings of the National Academy of Sciences *106*, 19017-19022. 10.1073/pnas.0908686106.

35. Bubb, M.R., Senderowicz, A.M., Sausville, E.A., Duncan, K.L., and Korn, E.D. (1994). Jasplakinolide, a cytotoxic natural product, induces actin polymerization and competitively inhibits the binding of phalloidin to F-actin. J Biol Chem *269*, 14869-14871. https://doi.org/10.1016/S0021-9258(17)36545-6.

36. Shoji, K., Ohashi, K., Sampei, K., Oikawa, M., and Mizuno, K. (2012). Cytochalasin D acts as an inhibitor of the actin-cofilin interaction. Biochem Biophys Res Commun *424*, 52-57. 10.1016/j.bbrc.2012.06.063.

37. Abbott, R.D., Koptiuch, C., Iatridis, J.C., Howe, A.K., Badger, G.J., and Langevin, H.M. (2013). Stress and matrix-responsive cytoskeletal remodeling in fibroblasts. J Cell Physiol *228*, 50-57. 10.1002/jcp.24102.

38. Matallanas, D., Birtwistle, M., Romano, D., Zebisch, A., Rauch, J., von Kriegsheim, A., and Kolch, W. (2011). Raf family kinases: old dogs have learned new tricks. Genes Cancer *2*, 232-260. 10.1177/1947601911407323.

39. Heidorn, S.J., Milagre, C., Whittaker, S., Nourry, A., Niculescu-Duvas, I., Dhomen, N., Hussain, J., Reis-Filho, J.S., Springer, C.J., Pritchard, C., and Marais, R. (2010). Kinase-dead BRAF and oncogenic RAS cooperate to drive tumor progression through CRAF. Cell *140*, 209-221. 10.1016/j.cell.2009.12.040.

40. Roberts, P.J., and Der, C.J. (2007). Targeting the Raf-MEK-ERK mitogen-activated protein kinase cascade for the treatment of cancer. Oncogene *26*, 3291-3310. 10.1038/sj.onc.1210422.

41. Crisp, M., Liu, Q., Roux, K., Rattner, J.B., Shanahan, C., Burke, B., Stahl, P.D., and Hodzic, D. (2006). Coupling of the nucleus and cytoplasm: role of the LINC complex. J Cell Biol *172*, 41-53. 10.1083/jcb.200509124.

42. Larsen, M., Artym, V.V., Green, J.A., and Yamada, K.M. (2006). The matrix reorganized: extracellular matrix remodeling and integrin signaling. Curr Opin Cell Biol *18*, 463-471. 10.1016/j.ceb.2006.08.009.

FIGURE LEGENDS

Figure 1. BRAFi induces nuclear deformation in CAFs.

(A) Representative confocal images showing nuclei stained with Hoechst in iM27 w/ or w/o PLX4032 treatment. Yellow circles highlight the approximate nuclear boundaries. iM27 cells were treated with either DMSO or PLX4032 for comparison.

(B–C) Scatter dot plots showing nuclear morphological parameters in iM27 w/ or w/o PLX4032 treatment. (B) the nuclear aspect ratio and (C) circularity were analyzed and quantified from confocal images using ImageJ. The data are presented as the means ± SDs (n = 40-46 nuclei per group).

(D–F) Confocal images showing immunostaining of key components of the LINC complex in iM27 w/ or w/o PLX4032 treatment, including (D) Nesprin-2, (E) SUN2, and (F) nuclear lamin A/C. In each figure, individual cells shown in small boxes are representative stained cells denoted by yellow boxes in the large boxes above. Disrupted distribution patterns of Nesprin-2, SUN2, and lamin A/C in PLX4032-treated iM27 cells are indicated by yellow arrows.

Figure 2. Mechanical association between actin polymerization and nuclear deformation leads to noncanonical β-catenin nuclear accumulation.

(A) Fluorescence images showing polymerized actin (F-actin) in normal human fibroblasts (NF#2) and iM27 cells. Phalloidin was used to label polymerized actin fibers.

(B) Quantification of F-actin intensity in NF#2 and iM27 cells. The data are presented as the means ± SDs (n = a minimum of 7-8 of random 20X fields).

(C) Fluorescence images showing polymerized F-actin in iM27 cells treated with DMSO or PLX4032.

(D) Quantification of F-actin intensity in DMSO-treated and PLX4032-treated iM27 cells. The data are presented as the means ± SDs (n=5-6 random 20X fields).

(E) Representative confocal images showing nuclei stained with Hoechst in iM27 cells treated with DMSO or Jaspla. Yellow circles highlight the approximate nuclear boundaries.

(F) Quantification of the nuclear morphological changes, including the nuclear aspect ratio (left) and circularity (right), analyzed and quantified from confocal images using ImageJ. The data are presented as the means ± SDs (n = 18 nuclei per group).

(G) Confocal images of F-actin in iM27 cells treated with DMSO or Jaspla. The representative individual cells shown in the insets correspond to the cells marked by yellow boxes in the larger images above. The actin caps are indicated by yellow arrows.

(H) Quantification of the actin cap intensity using ImageJ. The data are presented as the means ± SDs (n = 42 nuclei per group).

(I) Representative confocal images of Hoechst-stained nuclei in iM27 cells treated with DMSO, PLX4032, or the combination of PLX4032 and CytoD. Yellow circles highlight the approximate nuclear boundaries.

(J) Quantification of nuclear morphology, including the nuclear aspect ratio (left) and circularity (right), was performed, and the results were analyzed and quantified from confocal images via ImageJ. The data are presented as the means ± SDs (n = 26-39 nuclei per group).

(K) Confocal images of F-actin in iM27 cells treated with DMSO, PLX4032, or the combination of PLX4032 and CytoD. The representative individual cells shown in the insets correspond to the cells marked by yellow boxes in the larger images above. The actin caps are indicated by yellow arrows.

(L) Quantification of the actin cap intensity using ImageJ. The data are presented as the means ±

SDs (n = 30 nuclei per group).

(M-N) Confocal images showing SUN2 staining (M) and fluorescence microscopy images showing nuclear β-catenin staining (N) in iM27 cells treated with DMSO or Jaspla. Disrupted SUN2 distribution in Jaspla-treated iM27 cells is indicated by yellow arrows.

(O–P) Confocal images showing SUN2 staining (O) and fluorescence microscopy images showing nuclear β-catenin staining (P) in iM27 cells treated with PLX4032 or the combination of PLX4032 and CytoD. Yellow arrows indicate disorganized SUN2 distribution in iM27 cells treated with PLX4032 alone.

Figure 3. Matrix stiffness deforms the nucleus and regulates β-catenin nuclear entry

(A) Representative confocal images showing nuclei stained with Hoechst in iM27 cells cultured on soft slides with a stiffness of 0.2 kPa (left), hard slides with a stiffness of 50 kPa (middle), and hard slides with a stiffness of 50 kPa and CytoD treatment (right). Yellow circles highlight the approximate nuclear boundaries.

(B–C) Scatter dot plots showing the nuclear morphological changes in iM27 among three different conditions. (B) the nuclear aspect ratio and (C) circularity were analyzed and quantified from confocal images using ImageJ. The data are presented as the means ± SDs (n = 40 nuclei per group).

(D) Confocal images of F-actin in iM27 cells cultured on soft slides with a stiffness of 0.2 kPa (left), hard slides with a stiffness of 50 kPa (middle), and hard slides with a stiffness of 50 kPa and CytoD treatment (right). The representative individual cells shown in the insets correspond to the cells marked by yellow boxes in the larger images above. The actin caps are indicated by yellow arrows.

(E) Quantification of the actin cap intensity using ImageJ. The data are presented as the means ±

SDs (n = 25-30 nuclei per group).

(F) Confocal images showing SUN2 staining in iM27 cells cultured on soft slides with a stiffness of 0.2 kPa (left), hard slides with a stiffness of 50 kPa (middle), and hard slides with a stiffness of 50 kPa and CytoD treatment (right). Disorganized SUN2 distribution in iM27 cells cultured on 50 kPa slides is indicated by yellow arrows.

(G) Fluorescence microscopy images showing nuclear β-catenin staining in iM27 cells cultured on soft slides with a stiffness of 0.2 kPa (left), hard slides with a stiffness of 50 kPa (middle), and hard slides with a stiffness of 50 kPa and CytoD treatment (right).

(H) Quantification of nuclear β-catenin intensity in iM27 cells under three different conditions. The data are presented as the means ± SDs (n = 60 cells per group).

Figure 4. Nuclear β-catenin accumulation induces fibroblast reprogramming

(A) Schematic illustration of the melanoma mouse model used to study the *in vivo* effects of β-catenin-overexpressing fibroblasts on melanoma progression. D4M melanoma cells (green) were mixed with uninduced control fibroblasts (*Col1α2-CreER; Rosa-rtTA*, control melanoma) or mutant fibroblasts (*Col1α2-CreER; Rosa-rtTA; TetO-ΔN-β-catenin*, ΔN-β-catenin melanoma) and injected intradermally into the flanks of B6 mice. The tumors were allowed to grow until they reached approximately 62.5 mm^3 in volume. At this point (designated day 1), tamoxifen and doxycycline were administered to induce β-catenin overexpression in the mutant fibroblasts. Tumor growth was subsequently monitored daily until the end point.

(B) Tumor sizes were measured every other day and compared between control melanomas and ΔN-β-catenin melanomas (n = 8-9).

(C) Representative images of control melanomas and ΔN-β-catenin melanomas on day 18.

(D) Comparison of tumor weight between control melanomas and ΔN-β-catenin melanomas on day 18. Each data point represents the weight of an individual tumor. The data are presented as the means ± SDs (n = 8-9).

(E) H&E-stained control and ΔN-β-catenin melanoma tissue sections captured under a light microscope.

(F). Images show α-SMA and Ki67 immunofluorescence staining of control and ΔN-β-catenin melanoma tissue sections as indicated. The nuclei were counterstained with DAPI (blue).

(G) Comparison of the numbers of α-SMA- cells that were Ki67+ in each group. Each data point represents the number of α-SMA-; Ki67+ cells per mm^2 were counted for each melanoma sample. n = 15.

(H) Representative images of cyclin D1 staining of control and ΔN-β-catenin melanoma tissue sections from the indicated groups by immunohistochemistry.

(I) The graph shows the numbers of cyclin D1+ cells in each group. Each data point represents the number of cyclin D1+ cells per mm^2 counted for each melanoma sample. n = 13.

(J) Images showing α-SMA staining of control and ΔN-β-catenin melanoma tissue sections from respective group. The nuclei were counterstained with DAPI (blue).

(K) The graph shows the number of α-SMA+ cells in each group. Each data point represents the number of α-SMA cells per mm^2 counted for each melanoma sample. n = 18.

(L) Images showing collagen staining of melanoma tissue sections from the indicated groups.

(M) Quantitative comparison of collagen contents in control and ΔN-β-catenin melanoma tissue sections by collagen extraction and colorimetric measurement. n = 3.

(N) Immunohistochemistry images showing the expression of the ECM protein fibronectin in control and ΔN-β-catenin melanoma tissue sections as indicated.

(O) Quantitative comparison of the percentages of the surface areas occupied by fibronectin+ fibroblasts measured in control and ΔN-β-catenin melanoma tissue sections. Eleven to twelve random fields from three melanoma pairs were counted. n = 11-12.

For all the staining images, the scale bar represents 200 μm. In all the statistical graphs, the data are presented as the means ± SDs. *, P≤0.05; **, P≤0.01; ***, P≤0.001; ns, not significant.

Figure 5. BRAFi binds to the RAF kinase domain and promotes BRAF and CRAF dimerization and phosphorylation

(A) Western blot confirming effective silencing of ARAF, BRAF, or CRAF expression in iM27 cells using corresponding siRNAs.

(B) Representative fluorescence microscopy images showing β-catenin expression in iM27 cells transfected with scramble siRNA or siRNAs that deplete ARAF, BRAF, or CRAF expression under PLX4032 treatment. iM27 transfected with scramble siRNA without PLX4032 treatment were used as a control.

(C) Quantification of nuclear β-catenin intensity in iM27 and genetically modified iM27 cells as shown in (B) with or without PLX4032 treatment using ImageJ. The data are presented as the means ± SDs (n = 11 randomly selected 20 X fields per group).

(D) Representative PLA images showing BRAF-CRAF heterodimerization in DMSO- and PLX4032-treated iM27 cells. Red dots indicate BRAF-CRAF dimers.

(E) Quantification of PLA signals comparing PLX4032-treated iM27 cells with DMSO-treated iM27 cells. The data are presented as the means ± SDs (n = 9-10 randomly selected 40X fields per group).

(F) Representative PLA images showing BRAF-BRAF homodimerization in DMSO- and

PLX4032-treated iM27 cells. The red dots indicate BRAF-BRAF dimers.

(G) Quantification of PLA signals comparing PLX4032-treated iM27 cells with DMSO-treated iM27 cells. The data are presented as the means ± SDs (n = 9-10 randomly selected 40X fields per group).

(H) Representative PLA images showing CRAF-CRAF homodimerization in DMSO- and PLX4032-treated iM27 cells. The red dots indicate CRAF-CRAF dimers.

(I) Quantification of PLA signals comparing PLX4032-treated iM27 cells with DMSO-treated iM27 cells. The data are presented as the means ± SDs (n = 9-10 randomly selected 40X fields per group).

(J) Western blot analysis showing increased CRAF-CRAF and CRAF-BRAF interactions in PLX4032-treated iM27 cells compared with those in DMSO-treated iM27 cells. Co-IP was performed via the use of an anti-Myc antibody to pull down interacting proteins in iM27 cells coexpressing Myc-tagged and Flag-tagged CRAF.

(K-M) Western blot analysis of phosphorylated BRAF (Ser445) and CRAF (Ser338) expression in iM27 (K), BRAF-deficient iM27 overexpressing wild-type BRAF or BRAF (T529N) (L), and CRAF-deficient iM27 overexpressing wild-type CRAF or CRAF (T421N) (M) treated with either DMSO or PLX4032.

Figure 6. BRAFi-induced RAF activation and the nuclear accumulation of β-catenin are RAS dependent

(A) Western blot confirming effective silencing of KRAS, HRAS, and NRAS expression in iM27 using siRNAs.

(B) PLA results showing BRAF and CRAF heterodimerization in iM27 transfected with scramble

siRNA (Scr), scramble iM27 treaded with PLX4032, and RAS-deficient iM27 (siRASs) treated with PLX4032.

(C) Western blot showing the phosphorylation of BRAF (Ser445) and CRAF (Ser338) in iM27 transfected with scramble siRNA and RAS-deficient iM27 with and without PLX4032 treatment.

(D) Confocal images of nuclei visualized by Hoechst staining in iM27 transfected with scramble siRNA, scramble iM27 treaded with PLX4032, and RAS-deficient iM27 (siRASs) treated with PLX4032. The nuclear boundaries are outlined with yellow circles.

(E-F) Quantification of nuclear morphology based on the confocal images shown in (D), including the nuclear aspect ratio (E) and circularity (F), was performed via ImageJ. The data are presented as the means ± SDs (n = 30-67 nuclei per group).

(G) Confocal images of F-actin expression and organization in iM27 transfected with scramble siRNA, scramble iM27 treaded with PLX4032 (scramble), and RAS-deficient iM27 (siRASs) treated with PLX4032. Insets display enlarged views of representative individual cells (highlighted by yellow boxes). Yellow arrows indicate actin caps.

(H-I) Quantification of F-actin intensity (H) and actin cap intensity (I) using ImageJ. The data are presented as the means ± SDs (n = 6 randomly selected 20 X fields per group for H; n = 25-52 nuclei per group for I).

(J) Confocal images showing Nesprin-2 distribution in iM27 transfected with scramble siRNA, scramble iM27 treaded with PLX4032, and RAS-deficient iM27 (siRASs) treated with PLX4032. The yellow arrow indicates abnormal cytosolic localization of Nesprin-2.

(K) Representative fluorescence images showing nuclear β-catenin staining in iM27 transfected with scramble siRNA, scramble iM27 treaded with PLX4032, and RAS-deficient iM27 (siRASs) treated with PLX4032.

(L) Quantification of nuclear β-catenin intensity under the indicated conditions shown in (K). The data are presented as the means ± SDs (n = 9 randomly selected 20X fields per group).

Figure 7. ROCK signaling is downstream of RAF activation to promote cytoskeletal remodeling and nuclear deformation

(A) Western blot showing increased ERK phosphorylation in response to increasing concentrations of PLX4032 in iM27 cells.

(B) Western blot showing the phosphorylation of ERK in iM27 transfected with scramble siRNA and RAS-deficient iM27 (siRASs) with and without PLX4032 treatment.

(C-D) Western blots showing ERK phosphorylation in BRAF-deficient iM27 overexpressing wild-type BRAF and BRAF(T529N) (C) and in CRAF-deficient iM27 overexpressing wild-type CRAF and CRAF(T421N) (D) with and without PLX4032 treatment.

(E) Western blot showing increased phosphorylation of MYPT1 in PLX4032-treated iM27.

(F) Western blot showing the phosphorylation of MYPT1 in iM27 treated with DMSO, PLX4032, and a combination of PLX4032 and the ERK inhibitor SCH772984 (SCH).

(G) Representative confocal images of nuclear morphology visualized by Hoechst staining in iM27 treated with DMSO, PLX4032, and a combination of PLX4032 and the ROCK inhibitor Y27632.

(H-I) Quantification of nuclear morphology based on the confocal images shown in (G), including the nuclear aspect ratio (H) and circularity (I), was performed via ImageJ. The data are presented as the means ± SDs (n = 27-38 nuclei per group).

(J) Confocal images of F-actin expression and organization in iM27 treated with DMSO, PLX4032, and a combination of PLX4032 and the ROCK inhibitor Y27632. Insets display enlarged views of representative individual cells (highlighted by yellow boxes). Yellow arrows indicate the actin

caps.

(K) Quantification of the actin cap intensity via ImageJ shown in (J). The data are presented as the means ± SDs (n = 20 nuclei per group).

(L) Confocal images showing SUN2 distribution in iM27 treated with DMSO, PLX4032, and a combination of PLX4032 and the ROCK inhibitor Y27632. The yellow arrow indicates abnormal nuclear localization of SUN2 in PLX4032-treated cells.

(M) Representative fluorescence images showing nuclear β-catenin staining in iM27 treated with DMSO, PLX4032, and a combination of PLX4032 and the ROCK inhibitor Y27632.

(N) Quantification of the nuclear β-catenin intensity under the indicated conditions shown in (M). The data are presented as the means ± SDs (n = 40 nuclei per group).

Figure 8 ROCK inhibitor reverses stiffness-induced nuclear deformation and β-catenin accumulation.

(A) Representative confocal images showing nuclei stained with Hoechst in iM27 cells cultured on hard slides with a stiffness of 50 kPa with or without ROCK inhibitor Y27632 treatment. Yellow circles highlight the approximate nuclear boundaries.

(B–C) Scatter dot plots showing the nuclear morphological changes under the indicated conditions corresponding to (A). The nuclear aspect ratio (B) and circularity (C) were analyzed and quantified using ImageJ. The data are presented as the means ± SDs (n = 40 nuclei per group).

(D) Confocal images of F-actin expression and organization in iM27 cells cultured on hard slides with a stiffness of 50 kPa with or without ROCK inhibitor Y27632 treatment. The representative individual cells shown in the insets correspond to the cells marked by yellow boxes in the larger images above. The actin caps are indicated by yellow arrows.

(E) Quantification of the actin cap intensity using ImageJ shown in (D). The data are presented as the means ± SDs (n = 24-30 nuclei per group).

(F) Confocal images showing SUN2 staining in iM27 cells cultured on hard slides with a stiffness of 50 kPa with or without ROCK inhibitor Y27632 treatment. Disorganized SUN2 distribution in iM27 cells cultured on 50 kPa slides is indicated by yellow arrows.

(G) Fluorescence microscopy images showing nuclear β-catenin expression in iM27 cells cultured on hard slides with a stiffness of 50 kPa with or without ROCK inhibitor Y27632 treatment.

(H) Quantification of the nuclear β-catenin intensity in iM27 cells corresponding to (G). The data are presented as the means ± SDs (n = 60 cells per group).

Figure 9 A unique response mechanism by which CAFs respond to various external stimuli and reprogram transcriptional activities. The ROCK-cytoskeleton axis can be activated in CAFs by BRAFi and stiff substrates and drives nuclear deformation, which subsequently promotes increased β-catenin nuclear translocation and induces CAF reprogramming. Created with BioRender.com.

Figure 10 BRAFi accelerates BRAF and CRAF dimerization and transactivation in CAFs.

(A) In BRAF wild-type cells, without BRAFi treatment, RAF kinases are activated when a cell receives signals from its environment, usually through receptor tyrosine kinases (RTKs), and activate the small GTPase RAS. Activated RAS binds to BRAF and CRAF and releases autoinhibition, leading to RAF transactivation and the activation of downstream MEK and ERK.

(B) In BRAF-mutant cells, BRAF no longer needs activated RAS and can activate downstream MEK and ERK by itself. BRAFi inserts into the kinase domain of mutant BRAF and blocks its

activity.

(C) In BRAF wild-type CAFs, BRAF and CRAF still need activated RAS to prevent autoinhibition. However, BRAFi can insert into the kinase domains of BRAF and CRAF and induce abnormal conformational changes, which accelerate BRAF and CRAF dimerization and transactivation, leading to increased downstream MEK and ERK signaling activities.

Created with BioRender.com.

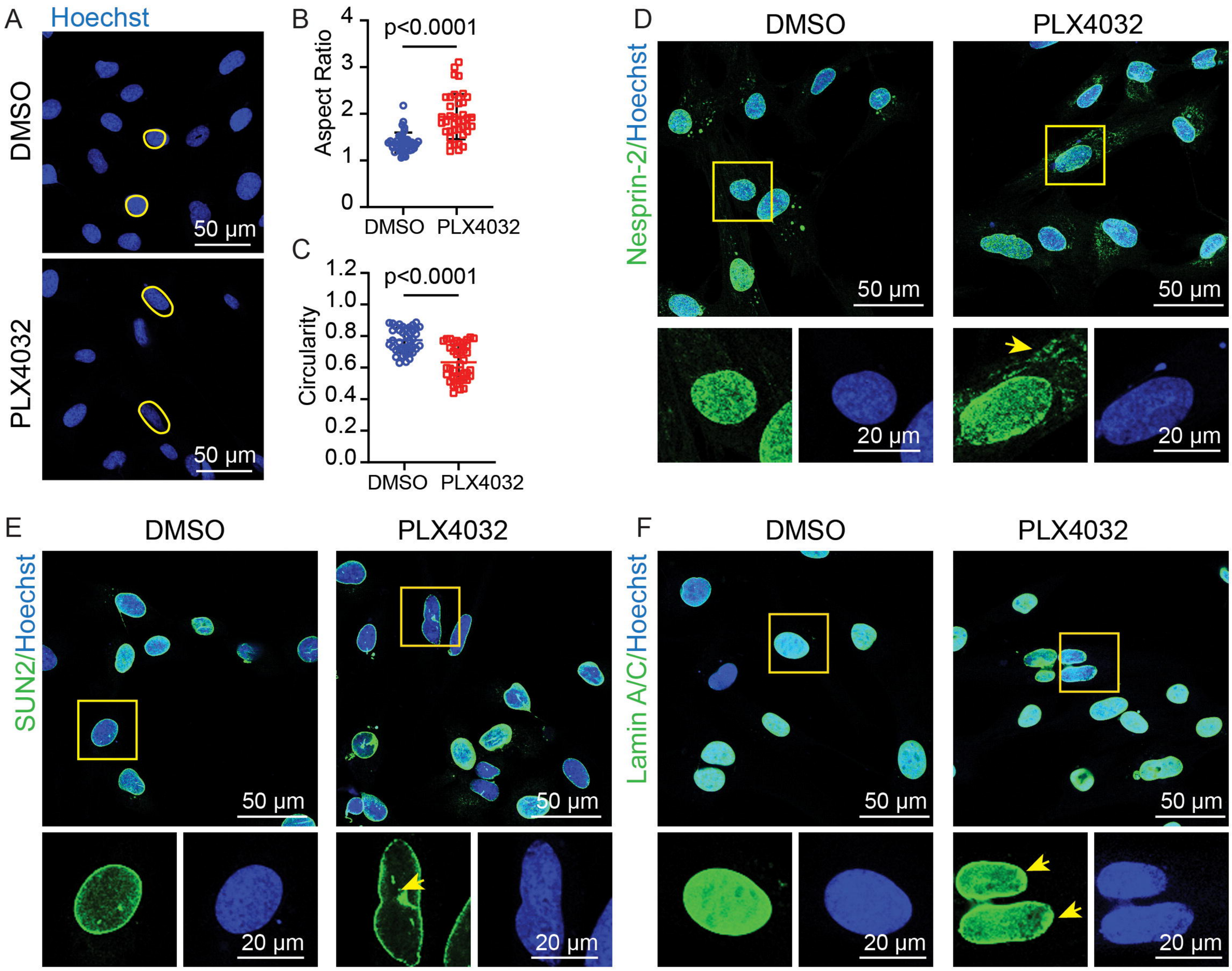
A
Hoechst
DMSO
PLX4032
50 µm
50 µm
B
p<0.0001
Aspect Ratio
4
3
2
1
0
DMSO
PLX4032
C
p<0.0001
Circularity
1.2
1.0
0.8
0.6
0.4
0.2
0.0
DMSO
PLX4032
D
DMSO
PLX4032
Nesprin-2/Hoechst
50 µm
50 µm
20 µm
20 µm
E
DMSO
PLX4032
SUN2/Hoechst
50 µm
50 µm
20 µm
20 µm
F
DMSO
PLX4032
Lamin A/C/Hoechst
50 µm
50 µm
20 µm
20 µm

Figs. 1

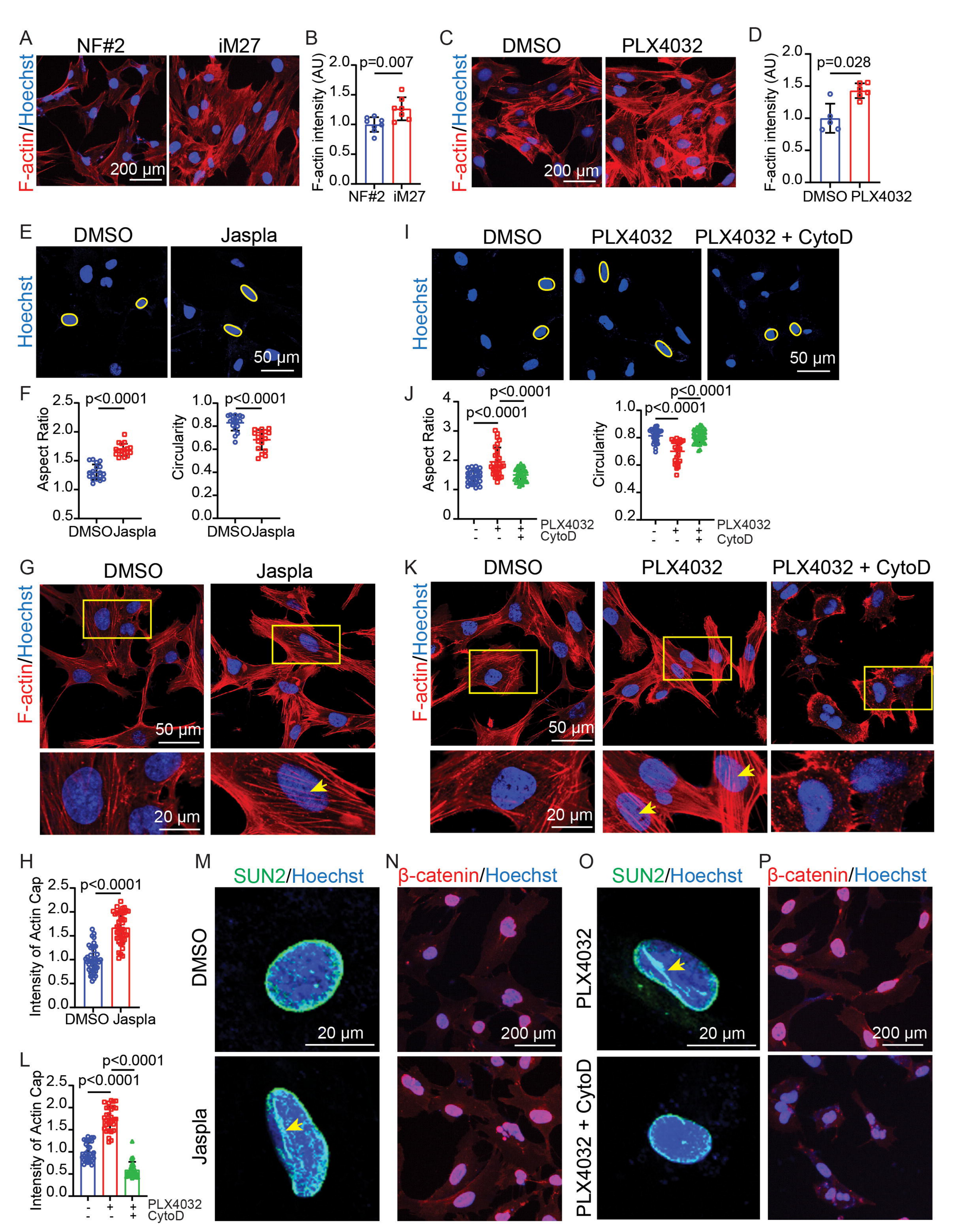
A
NF#2
iM27
F-actin/Hoechst
200 µm
B
F-actin intensity (AU)
p=0.007
NF#2 iM27
C
DMSO
PLX4032
F-actin/Hoechst
200 µm
D
F-actin intensity (AU)
p=0.028
DMSO PLX4032
E
DMSO
Jaspla
Hoechst
50 µm
F
Aspect Ratio
p<0.0001
DMSO Jaspla
Circularity
p<0.0001
DMSO Jaspla
G
DMSO
Jaspla
F-actin/Hoechst
50 µm
20 µm
H
Intensity of Actin Cap
p<0.0001
DMSO Jaspla
I
DMSO
PLX4032
PLX4032 + CytoD
Hoechst
50 µm
J
Aspect Ratio
p<0.0001
p<0.0001
PLX4032
CytoD
Circularity
p<0.0001
p<0.0001
PLX4032
CytoD
K
DMSO
PLX4032
PLX4032 + CytoD
F-actin/Hoechst
50 µm
20 µm
L
Intensity of Actin Cap
p<0.0001
p<0.0001
PLX4032
CytoD
M
SUN2/Hoechst
DMSO
Jaspla
20 µm
N
β-catenin/Hoechst
200 µm
O
SUN2/Hoechst
PLX4032
PLX4032 + CytoD
20 µm
P
β-catenin/Hoechst
200 µm

Fig 2

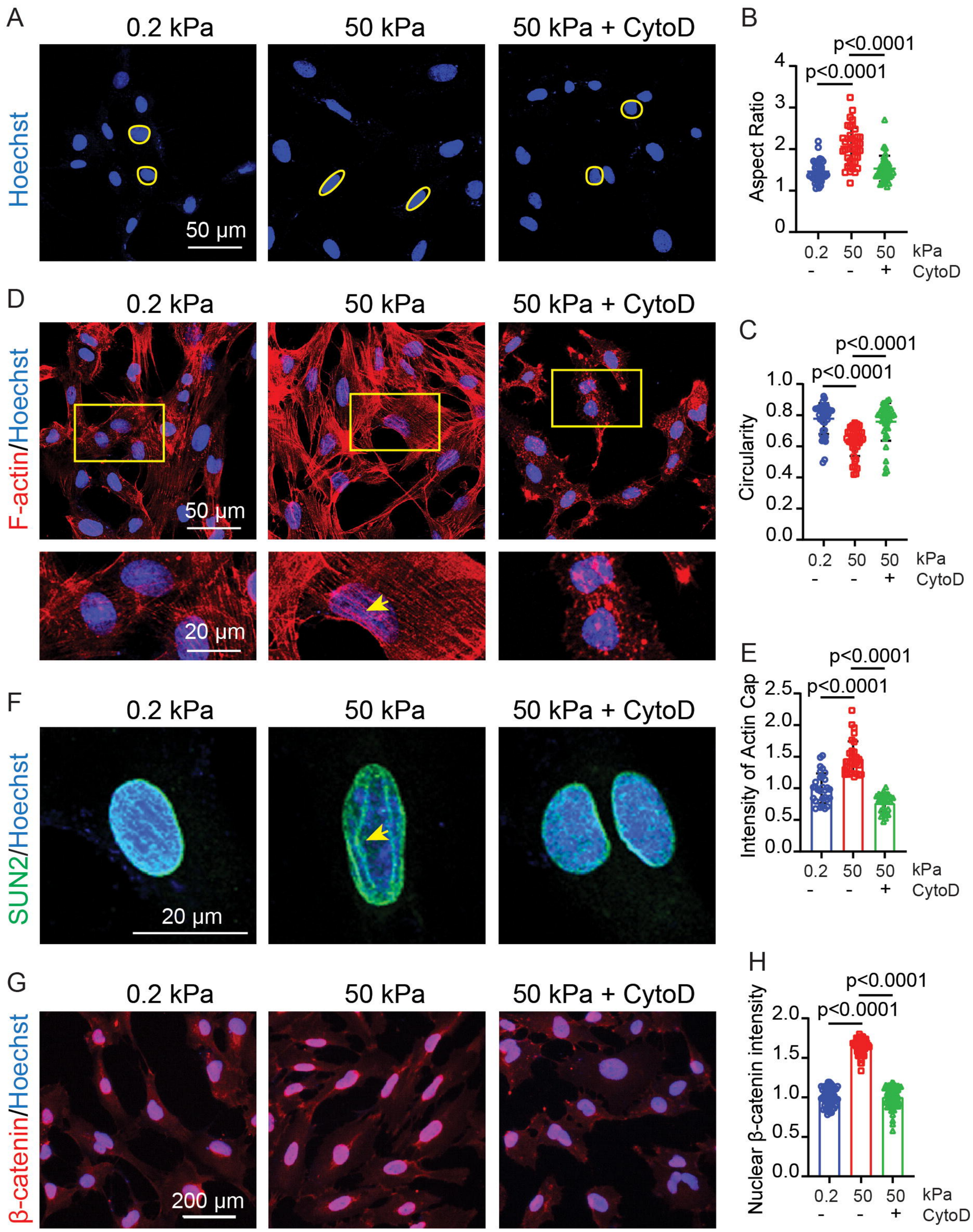
A
0.2 kPa
50 kPa
50 kPa + CytoD
Hoechst
50 µm
B
p<0.0001
p<0.0001
Aspect Ratio
0.2 50 50 kPa
- - + CytoD
D
F-actin/Hoechst
20 µm
C
Circularity
E
Intensity of Actin Cap
F
SUN2/Hoechst
G
β-catenin/Hoechst
200 µm
H
Nuclear β-catenin intensity

Fig 3

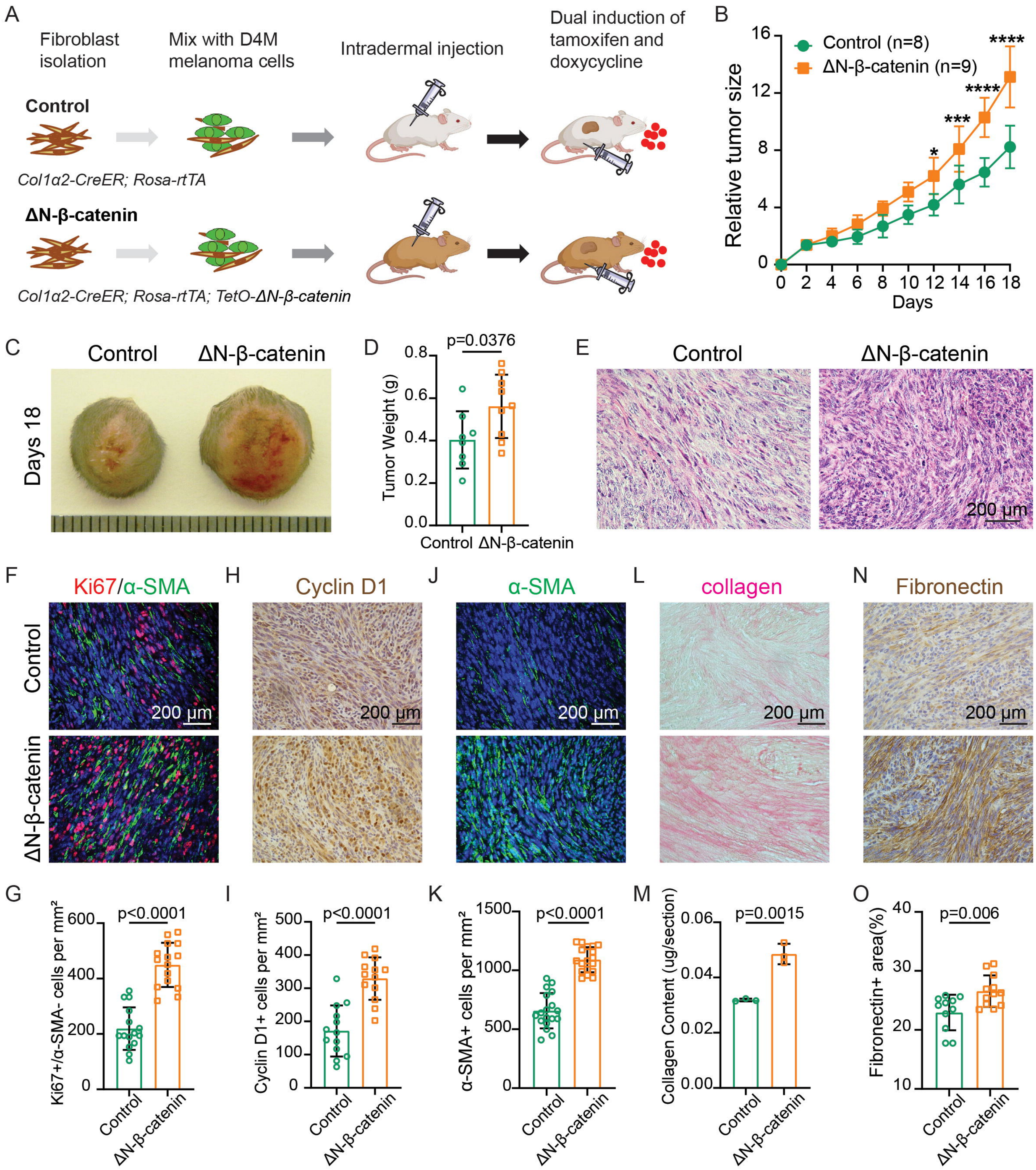
A
Fibroblast isolation
Mix with D4M melanoma cells
Intradermal injection
Dual induction of tamoxifen and doxycycline
Control
Col1α2-CreER; Rosa-rtTA
ΔN-β-catenin
Col1α2-CreER; Rosa-rtTA; TetO-ΔN-β-catenin
B
Control (n=8)
ΔN-β-catenin (n=9)
Relative tumor size
Days
C
Control
ΔN-β-catenin
Days 18
D
p=0.0376
Tumor Weight (g)
Control
ΔN-β-catenin
E
Control
ΔN-β-catenin
200 μm
F
Ki67/α-SMA
Control
ΔN-β-catenin
200 μm
H
Cyclin D1
J
α-SMA
L
collagen
N
Fibronectin
G
p<0.0001
Ki67+/α-SMA- cells per mm²
I
p<0.0001
Cyclin D1+ cells per mm²
K
p<0.0001
α-SMA+ cells per mm²
M
p=0.0015
Collagen Content (ug/section)
O
p=0.006
Fibronectin+ area(%)

Fig 4

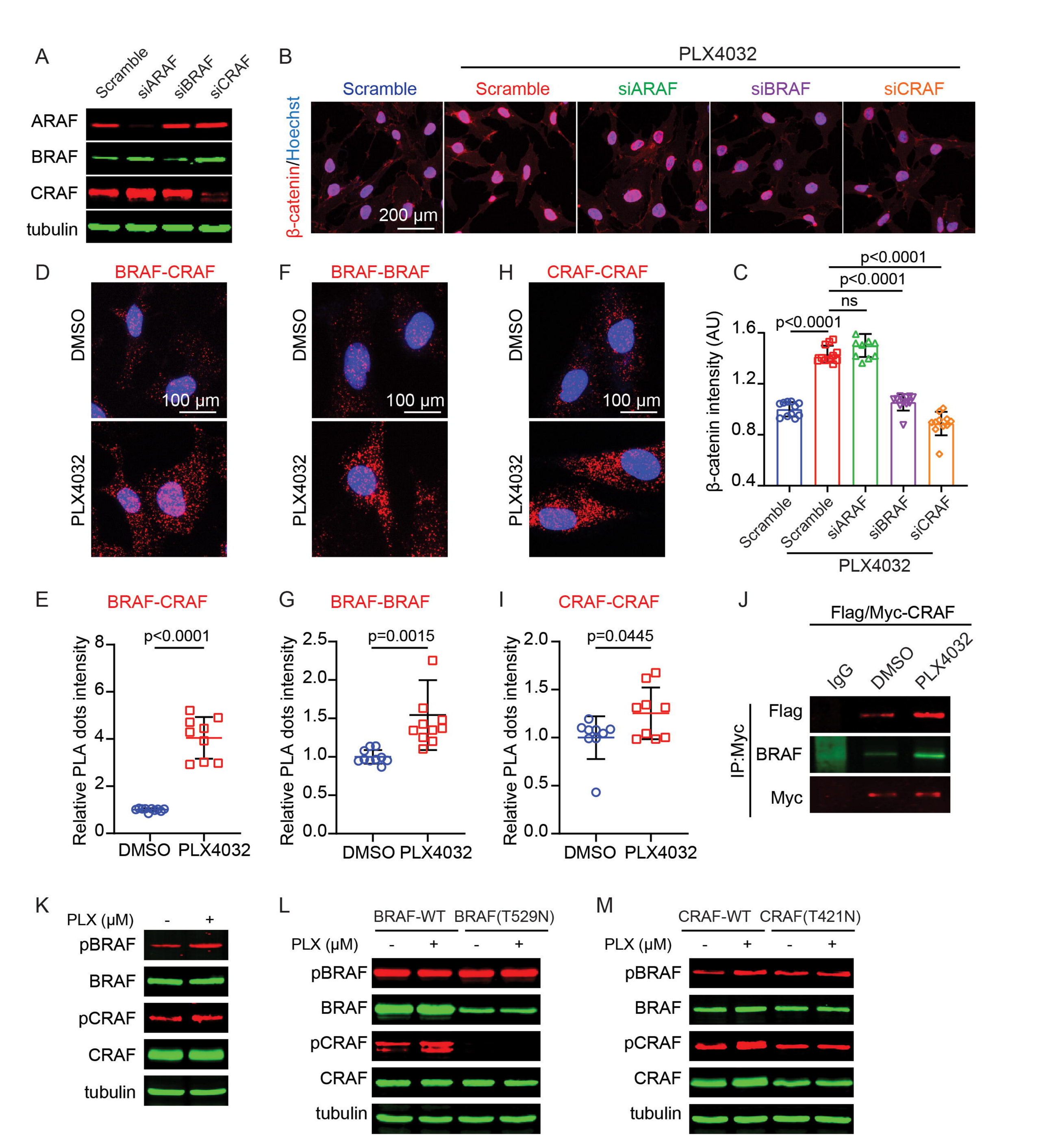
A
Scramble
siARAF
siBRAF
siCRAF
ARAF
BRAF
CRAF
tubulin
B
PLX4032
Scramble
Scramble
siARAF
siBRAF
siCRAF
β-catenin/Hoechst
200 μm
C
p<0.0001
p<0.0001
ns
p<0.0001
β-catenin intensity (AU)
1.6
1.2
0.8
0.4
Scramble
Scramble
siARAF
siBRAF
siCRAF
PLX4032
D
BRAF-CRAF
DMSO
PLX4032
100 μm
F
BRAF-BRAF
DMSO
PLX4032
100 μm
H
CRAF-CRAF
DMSO
PLX4032
100 μm
E
BRAF-CRAF
p<0.0001
Relative PLA dots intensity
8
6
4
2
0
DMSO
PLX4032
G
BRAF-BRAF
p=0.0015
Relative PLA dots intensity
2.5
2.0
1.5
1.0
0.5
0.0
DMSO
PLX4032
I
CRAF-CRAF
p=0.0445
Relative PLA dots intensity
2.0
1.5
1.0
0.5
0.0
DMSO
PLX4032
J
Flag/Myc-CRAF
IgG
DMSO
PLX4032
IP:Myc
Flag
BRAF
Myc
K
PLX (μM)
-
+
pBRAF
BRAF
pCRAF
CRAF
tubulin
L
BRAF-WT
BRAF(T529N)
PLX (μM)
-
+
-
+
pBRAF
BRAF
pCRAF
CRAF
tubulin
M
CRAF-WT
CRAF(T421N)
PLX (μM)
-
+
-
+
pBRAF
BRAF
pCRAF
CRAF
tubulin

Fig 5

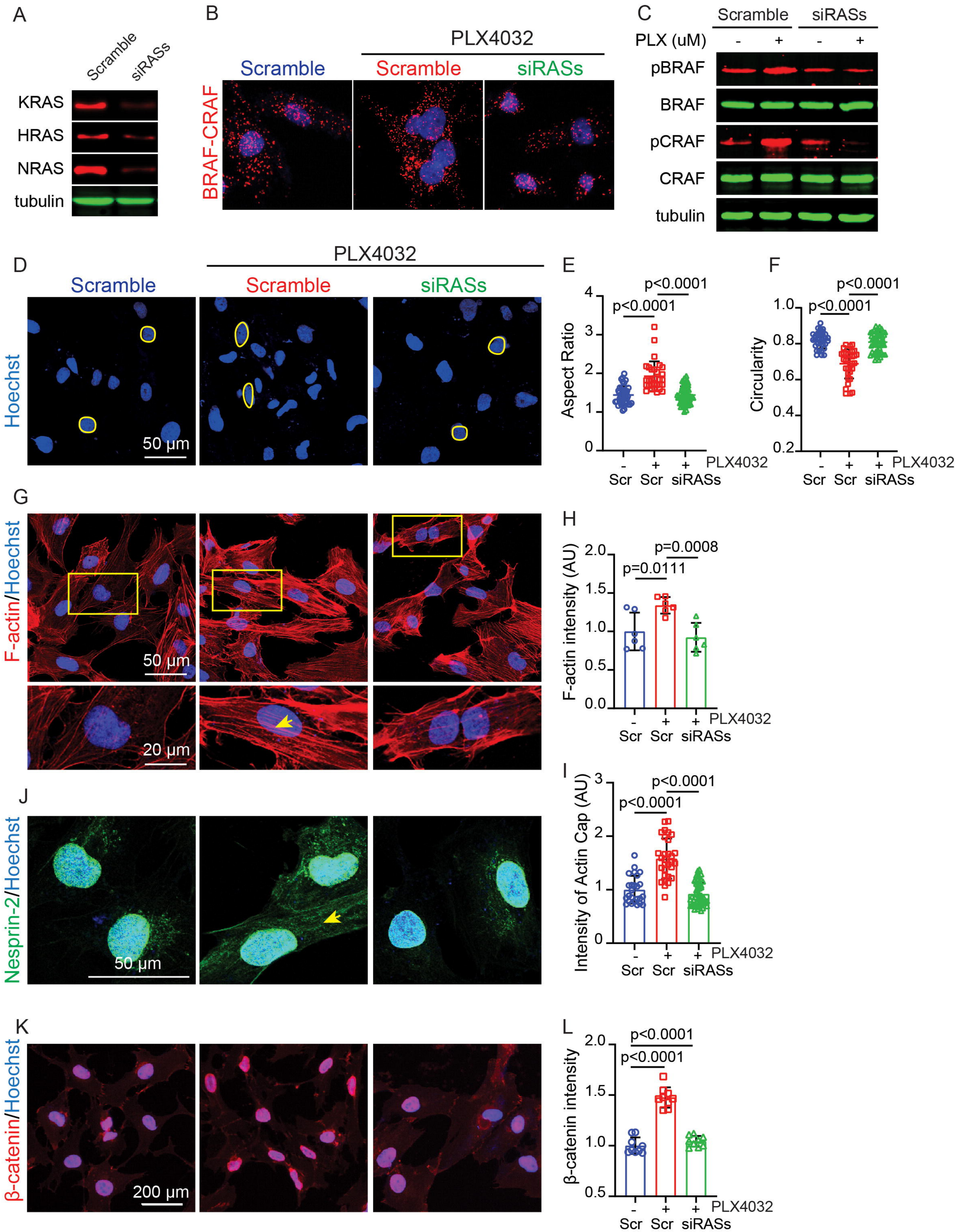
A
Scramble
siRASs
KRAS
HRAS
NRAS
tubulin
B
PLX4032
Scramble
Scramble
siRASs
BRAF-CRAF
C
Scramble
siRASs
PLX (uM)
- + - +
pBRAF
BRAF
pCRAF
CRAF
tubulin
D
PLX4032
Scramble
Scramble
siRASs
Hoechst
50 µm
E
p<0.0001
p<0.0001
Aspect Ratio
PLX4032
Scr Scr siRASs
F
p<0.0001
p<0.0001
Circularity
PLX4032
Scr Scr siRASs
G
F-actin/Hoechst
50 µm
20 µm
H
p=0.0008
p=0.0111
F-actin intensity (AU)
PLX4032
Scr Scr siRASs
I
p<0.0001
p<0.0001
Intensity of Actin Cap (AU)
PLX4032
Scr Scr siRASs
J
Nesprin-2/Hoechst
50 µm
K
β-catenin/Hoechst
200 µm
L
p<0.0001
p<0.0001
β-catenin intensity
PLX4032
Scr Scr siRASs

Figs. 6

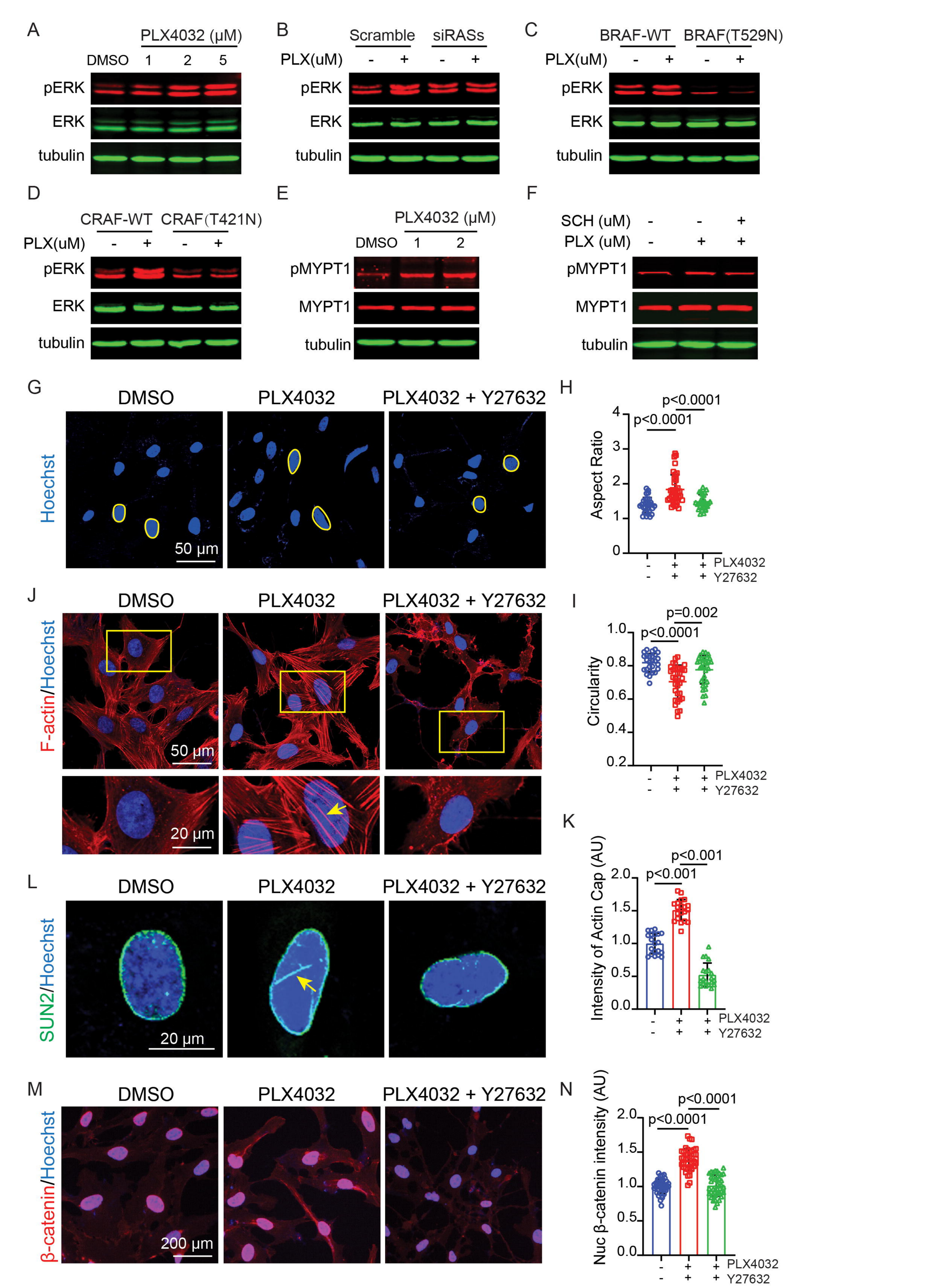
A
PLX4032 (μM)
DMSO 1 2 5
pERK
ERK
tubulin
B
Scramble siRASs
PLX(uM) - + - +
pERK
ERK
tubulin
C
BRAF-WT BRAF(T529N)
PLX(uM) - + - +
pERK
ERK
tubulin
D
CRAF-WT CRAF(T421N)
PLX(uM) - + - +
pERK
ERK
tubulin
E
PLX4032 (μM)
DMSO 1 2
pMYPT1
MYPT1
tubulin
F
SCH (uM) - - +
PLX (uM) - + +
pMYPT1
MYPT1
tubulin
G
DMSO
PLX4032
PLX4032 + Y27632
Hoechst
50 μm
H
p<0.0001
p<0.0001
Aspect Ratio
0 1 2 3 4
- + + PLX4032
- + + Y27632
J
DMSO
PLX4032
PLX4032 + Y27632
F-actin/Hoechst
50 μm
20 μm
I
p=0.002
p<0.0001
Circularity
0.2 0.4 0.6 0.8 1.0
- + + PLX4032
- + + Y27632
K
p<0.001
p<0.001
Intensity of Actin Cap (AU)
0.0 0.5 1.0 1.5 2.0
- + + PLX4032
- + + Y27632
L
DMSO
PLX4032
PLX4032 + Y27632
SUN2/Hoechst
20 μm
M
DMSO
PLX4032
PLX4032 + Y27632
β-catenin/Hoechst
200 μm
N
p<0.0001
p<0.0001
Nuc β-catenin intensity (AU)
0.0 0.5 1.0 1.5 2.0
- + + PLX4032
- + + Y27632

Figs. 7

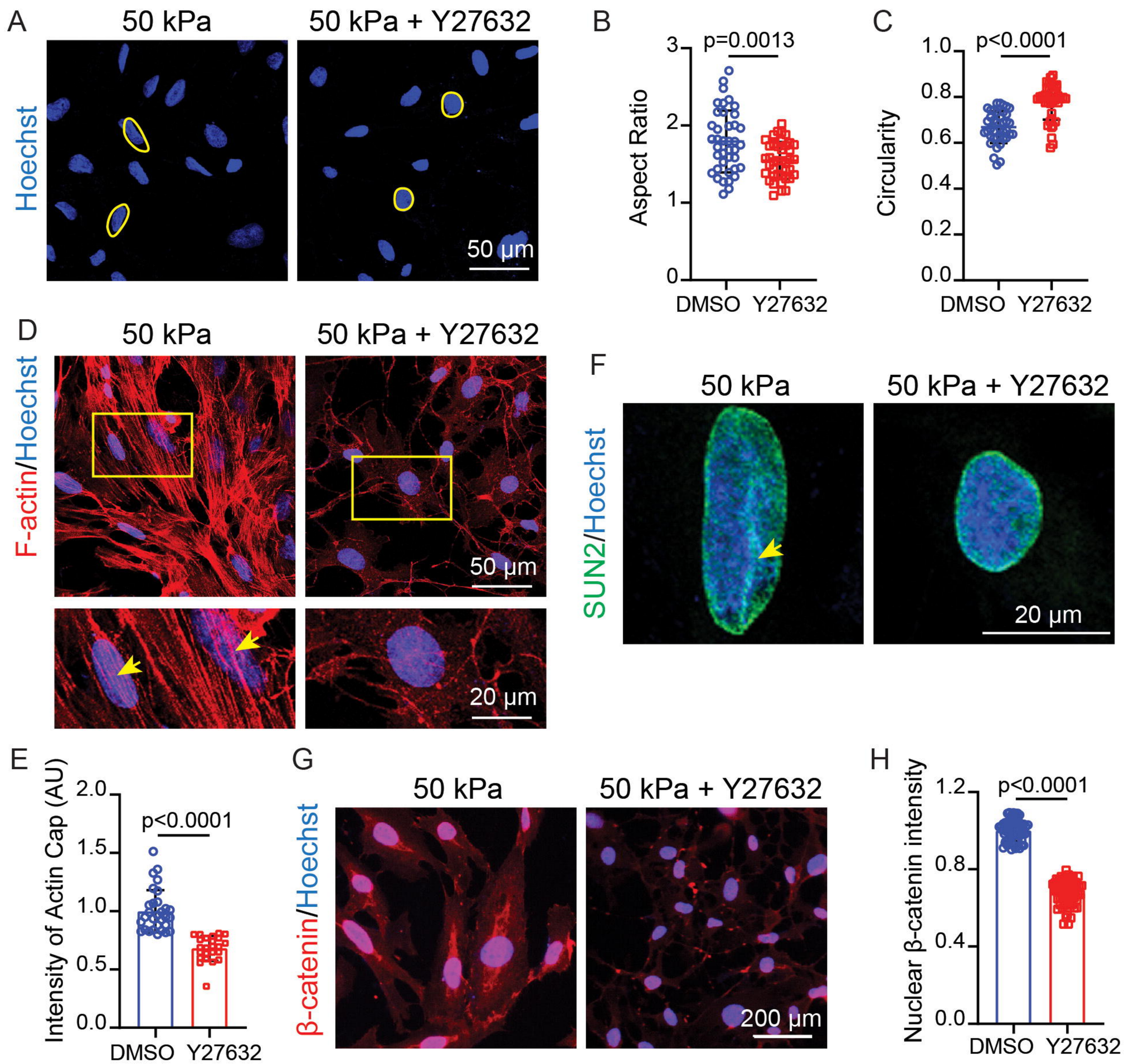
A
50 kPa
50 kPa + Y27632
Hoechst
50 µm
B
p=0.0013
Aspect Ratio
DMSO
Y27632
C
p<0.0001
Circularity
DMSO
Y27632
D
50 kPa
50 kPa + Y27632
F-actin/Hoechst
50 µm
20 µm
F
50 kPa
50 kPa + Y27632
SUN2/Hoechst
20 µm
E
p<0.0001
Intensity of Actin Cap (AU)
DMSO
Y27632
G
50 kPa
50 kPa + Y27632
β-catenin/Hoechst
200 µm
H
p<0.0001
Nuclear β-catenin intensity
DMSO
Y27632

Fig 8

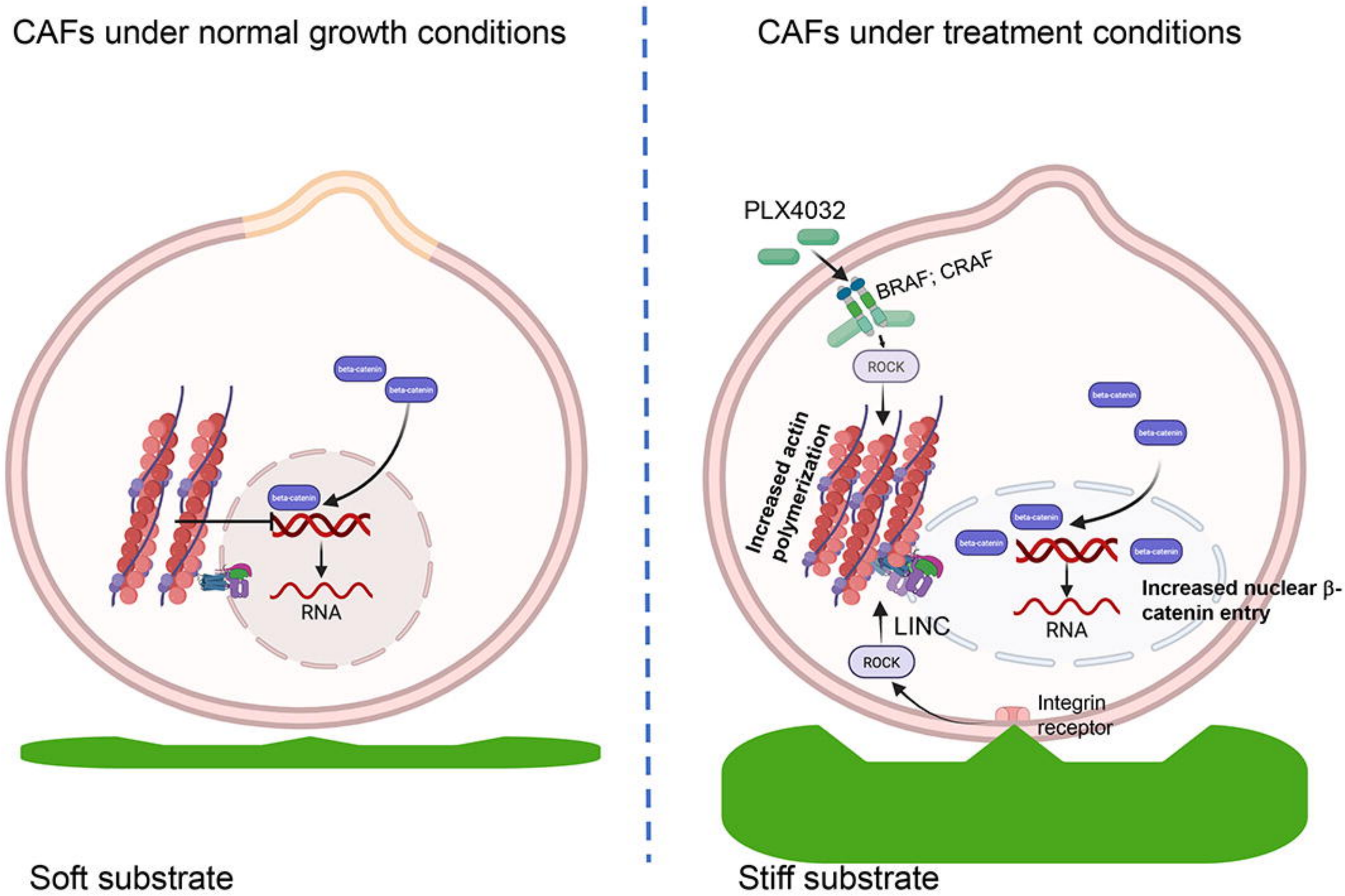
CAFs under normal growth conditions
CAFs under treatment conditions
beta-catenin
RNA
PLX4032
BRAF; CRAF
ROCK
Increased actin polymerization
LINC
ROCK
Integrin receptor
Increased nuclear β-catenin entry
Soft substrate
Stiff substrate

Fig. 9

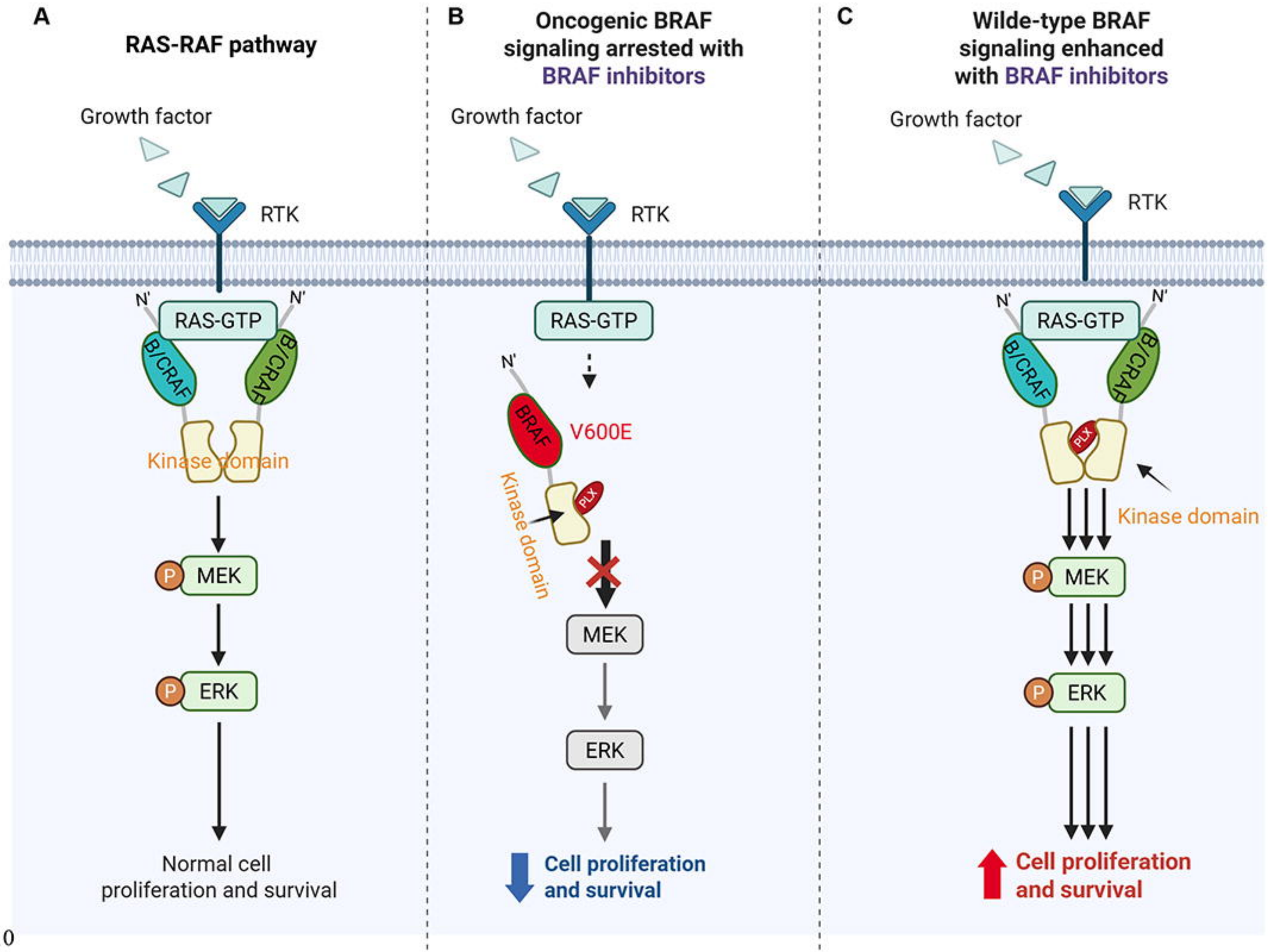
A
RAS-RAF pathway
Growth factor
RTK
N'
N'
RAS-GTP
B/CRAF
B/CRAF
Kinase domain
P
MEK
P
ERK
Normal cell
proliferation and survival
B
Oncogenic BRAF
signaling arrested with
BRAF inhibitors
Growth factor
RTK
RAS-GTP
N'
BRAF
V600E
Kinase domain
PLX
MEK
ERK
Cell proliferation
and survival
C
Wilde-type BRAF
signaling enhanced
with BRAF inhibitors
Growth factor
RTK
N'
N'
RAS-GTP
B/CRAF
B/CRAF
PLX
Kinase domain
P
MEK
P
ERK
Cell proliferation
and survival

Fig. 10